Microdynamics of Complex Fluids: Yield Stress in Chitosan Solutions and Active Colloids

by

Nina Gasbarro

A dissertation submitted in partial fulfillment
of the requirements for the degree of
Doctor of Philosophy
(Chemical Engineering)
in the University of Michigan
2020

Doctoral Committee:

Professor Michael J. Solomon, Chair
Professor Ronald Larson
Professor Anish Tuteja
Professor Robert Ziff

Nina Gasbarro

nmgasb@umich.edu

ORCID ID: 0000-0002-7001-6628

Dedication

This dissertation is dedicated to Cornelius Cilliers.

Acknowledgments

The completion of this Ph.D. would not have been possible without the support and assistance of countless colleagues, friends, and family. I consider myself very lucky to have found such talented and kind people.

First, I would like to express my deepest appreciation to Dean Michael J. Solomon for his guidance throughout my years. At critical moments, Mike's support and kindness were critical in enabling the continuation of my Ph.D. Although at first I must admit that I did not, I have come to appreciate and admire his thoroughness and rigor as a scientist. As a result of Mike's dedication to quality, I have yet to see anything but impeccable work published from the group, and I feel I have received the highest quality training possible. I know that this gift will continue to manifest in my future endeavors, and I will continue to be grateful for my time with Mike. I would also like to thank my committee of Professor Ronald Larson, Professor Anish Tuteja, and Professor Robert Ziff, especially for their flexibility and accommodation of my defense on an expedited timeframe.

Second, I would like to thank my fiancé Cornelius Cilliers for his unwavering support and encouragement through truly challenging times, without which this Ph.D. would not have been possible. I do not believe anything in this world is dark enough to escape the luminosity of your kindness, love and laughter. Also, I'm extremely grateful for the love and openness your

family has extended to me. Corietha, Johannes, Renée, Aaron, Hannes, and Kim – thank you for including me in your reunions, vacations and holidays. Lastly, I am very thankful that you picked Horace. I have to admit that I was skeptical about adopting a 20 lbs. cat with dental issues of unknown age, but I could not have been more wrong. Horace has brought joy and unexpected support in finishing my Ph.D. with his constant need to cuddle. I love you, and I cannot wait to spend my life with you.

Thirdly, I'm indebted to the friends and family that have supported me through this long process. I would like to thank my mother Susan Gasbarro for her generosity that made finishing and moving to San Diego possible. Also, special thanks to Katie Brown for always being a bird. I'd also like to acknowledge Keara Saud as a wonderful lab mate and friend. As a collaborator, I truly admire your work ethic and careful consideration of details. As a friend, I will never forget the kindness and generosity that Colin and you extended to me after my car accident. I would also like to thank my former officemate Carlos Silvera for such insightful conversation and life advice. Further, I would like to thank the Solomon Lab past and present, especially Mahesh Ganesan and Yufei Wei for their excellent technical insight.

Table of Contents

List of Figures

Abstract

In this dissertation, we study the role of microstructure and microdynamics in determining the functional properties of soft matter using rheology, dynamic light scattering (DLS), and particle-tracking video microscopy. This role is considered in two systems: aqueous solutions of chitosan and active Janus microspheres. The microdyanmical characterization of complex solutions is of broad scientific interest as understanding solution microstructure enables the prediction and manipulation of macroscopic properties. For chitosan, solution rheology is explored to probe the existence of an apparent yield stress. The possibility of shear-banded flow is investigated using a rheo-optical setup, and the quiescent microstructure of concentrated solutions is characterized using DLS. For active Janus microspheres, the microdynamics are characterized using DLS as a novel investigative technique.

The macroscopic rheology of chitosan solutions features shear thinning at low shear rates consistent with the existence of an apparent yield stress. At shear rates above yielding, a constant viscosity plateau is observed with concentration-dependent scaling consistent with existing models of entangled and associating polymers below the gel point. The concentration-dependent scaling of the apparent yield stress, $\sigma_0(c) \sim c^{2.8\pm0.2}$ in the concentration range c = 7.50-65.0 mg/mL, is consistent with a solution microstructure of fractal clusters of fractal dimension $d_f = 1.6\pm0.2$. The addition of urea, a hydrogen bond and hydrophobic interaction disrupter, did not change the reported concentration-dependent scaling of the apparent yield stress or the

plateau viscosity but did weaken the apparent yield stress magnitude by ~30% on average. The microdynamics of a concentrated chitosan solution and a weak chitosan gel were characterized by DLS. The extracted slow microdynamics are consistent with the presence of a structured network or glassy fluid.

To evaluate the possibility of shear banded flow of chitosan solutions in the shear rate range of the apparent yield stress, a rheo-optical instrument was used to measure the velocity profile in the gap between parallel plates. Silicone oil was applied around the gap to prevent rapid sample evaporation but resulted in image distortion as well as new secondary flows. To validate our modified experimental conditions, we carefully evaluate lower stress and shear rate limits using standard solutions. We find that in the experimentally valid shear rate range of $\dot{\gamma}$ = 0.01-0.056 1/s chitosan solutions do not exhibit shear banding. The shear rate range of characterization, although significantly lower than most literature measurements, does not completely rule out the possibility of shear banding in self-associating chitosan solutions.

The microdynamics of active colloids were characterized using DLS as a novel investigative tool. In the presence of hydrogen peroxide, Janus microspheres of platinum and polystyrene undergo active motion by means of self-diffusiophoresis. The dynamic structure factor decays more steeply with increasing hydrogen peroxide concentration, suggestive of non-diffusive microdynamics and propulsion. A model that combines active motion with passive diffusion is developed to extract v* from the dynamic structure factor. For hydrogen peroxide concentrations of 1-10 vol.%., particles of d = 0.7 μm and d = 1.2 μm have v* = 4-16 μm/s and v* = 2-13 μm/s respectively. Comparison with v* from direct measurements using confocal

microscopy and particle tracking was limited by anomalies in the optical microscopy and particle tracking data. However, external measurements of v* from confocal microscopy and particle tracking agree with v* determined from DLS measurements.

Chapter 1

Introduction

1.1 Introduction

In this dissertation, we characterize the microstructure and microdynamics of two systems of chitosan and active Janus microspheres. The microdynamics of a system are determined by the motion of particles or polymers on the microscopic scale. The summation of these movements ultimately determines macroscopic rheological properties that are directly observable. The microdyanmical characterization of complex solutions is of broad scientific interest as understanding the solution microstructure can enable the prediction and manipulation of macroscopic properties. For example, fluid mixtures of cornstarch and water thicken into a solid-like paste under impact. This seemingly counterintuitive behavior can be understood from the solution microdynamics. In order to flow, the grains of cornstarch must roll past each other. In response to a sudden impact, the grains are confined and cannot move, leading to the observed solid-like behavior.[2]

Complex fluids are used in a wide range of applications including consumer goods, biomedical applications, food science and coatings. The properties of these fluids may control the quality of the final product. Chitosan based complex fluids are of particular interest due to the favorable intrinsic properties of chitosan. Chitosan is biodegradable,[3] exhibits low toxicity in the μg/mL concentration range[4] and can be easily derrivatized. Also, chitosan is often sourced from seafood industry waste, making it an environmentally friendly material.

Active motion may enable the design of functional fluids with a high degree of specificity. Active colloids can be endlessly customized, enabling application-specific tailoring. For example, the surface of active colloids can be functionalized to strongly interact with a specific target. Surface functionalization of active particles has been successfully utilized in the self-repair of electrical circuits,[5] self-assembly of artificial tissue,[6] and drug delivery.[7] Also, active motion allows faster transport than passive diffusion. Supra-diffusive motion may be utilized in applications requiring rapid transport and contact with targets, as in environmental remediation.[8]

For chitosan solutions, a quiescent aggregate microstructure has been reported,[9,10] while the rheological behavior at low shear rates has been unexplored. This low shear-rate regime is of fundamental interest because low shear stresses potentially couple to weak or transient microstructures. In Chapter 2, we characterize the microstructure of quiescent solutions with DLS and the rheology of the low shear rate regime. In Chapter 3, we probe the effect of chitosan solution microstructure on flow. Rheo-optical flow characterization is used to evaluate the possibility of shear banding.

For solutions of active colloids, motion has been characterized using microscopy coupled with particle tracking to extract the mean squared displacement (ΔL^2).[11–13] While simple in conception to execute, the utility of this methodology is limited to particles of sufficient size for optical resolution and image analysis. Also, the motion of tracked particles is constrained to the imaged plain, and, thus, the extracted ΔL^2 is two-dimensional, which may not accurately

describe the motion of active particles in bulk solutions. In Chapter 4, we show that DLS can be used to successfully characterize colloidal active motion.

In this introduction, we introduce background information relevant to addressing these research aims. First, a detailed description of chitosan nomenclature, properties, and applications is presented to provide context for Chapters 2 and 3. Second, we outline general rheological techniques with emphasis on tests performed on chitosan solutions in Chapter 2. Third, we provide a general introduction to DLS for understanding its utilization in Chapters 2 and 4. Fourth, to contextualize flow measurements in Chapter 3, we provide an introduction to shear banding and the techniques used to characterize it. Fifth, we introduce active motion by building on passive colloidal motion and introducing characterization techniques.

1.2 Chitosan properties and applications

1.2.1 Chitosan composition and microstructure

Chitosan is a de-acetylated derivative of the naturally occurring biopolymer chitin. Chitosan is a copolymer of β-(1→4)-linked D-glucosamine ($C_6H_{13}NO_5$) and N-acetyl-D-glucosamine ($C_8H_{15}NO_6$); the fraction and distribution of acetylated groups varies. The degree of acetylation (DA) describes the fraction of acetylated groups in chitosan. Typical DA values for chitosan range from 0-0.4 and for chitin from 0.4-1. The distinction between chitin and chitosan is not based on DA but solubility under mild acidic solutions (pH < 6.1).[14] The enhanced solubility of chitosan is due to the protonation of amino groups at low DA's. The chitosan used in Chapters 2 and 3 of this thesis has a DA of 0.28, shown as a yellow diamond in Figure 1.1.

Figure 1.1 Spectrum of DA for chitin and chitosan. The yellow diamond represents DA = 0.28 for the chitosan used in Chapters 2 and 3.

Chitosan is both a hydrogen bond acceptor and donor and is also subject to hydrophobic effects. Microcrystalline domains of glucosamine have been hypothesized to underlie chitosan aggregation, but direct observation of glucosamine crystallinity has been limited to chitosan powders.[15] As a result of these interactions, chitosan solutions are prone to self-association. Aggregates in chitosan solutions have been imaged by wet-STEM,[10] TEM[9,10,16] and SEM.[10,17] In fact, TEM micrographs of dilute chitosan show a dense core and a loose shell with dangling chains[9] that become increasingly interconnected as concentration increases.[10]

1.2.2 Chitosan as an emerging biomaterial

Chitosan has applications in multiple fields and industries. It is easily derivatized, so as to tune its properties for specific applications. Also, chitosan is biodegradable,[3] antimicrobial,[18,19] and antifungal.[19,20] Chitosan exhibits low toxicity in the μg/mL concentration range[4] and is used as a food additive.[21] Chitosan derivatives have been incorporated into cosmetics and consumer goods formulations.[22,23] Further, there is potential for applications of chitosan in drug delivey,[24] wastewater treatment,[25] bio-fabrication,[26] and tissue engineering.[1]

The intrinsic properties of chitosan are well suited for skin healing. In addition to biocompatibility and antimicrobial properties, chitosan is an hemostatic agent, meaning that it

binds with red blood cells and rapidly clots blood.[27,28] Also, chitosan enhances the function of inflammatory cells, promoting the granulation and organization of healing skin cells.[29] Moreover, chitosan and chitosan derivatives can be used to deliver antibiotics such as amikacin,[30,31] vancomycin,[31,32] minocycline[33] and gentamicin[34] to target areas to prevent and treat infection.[28] Chitosan based topical bandages are already commercially available such as, for example, the HemCon® Bandage from Tricol Biomedical Inc. Future chitosan-based medical technologies may utilize the implantation of biodegradable chitosan-based sponges or patches that do not need to be surgically removed.[34,35]

1.3 Rheological characterization of complex fluids

Mechanical properties are an important consideration in the development and implementation of new technologies. For example, in the previously discussed example of chitosan-based topical medical bandages, bandages must be sturdy enough to protect wounds but flexible enough to remain in tact when sheared or stressed as a result of normal patient movement. Rheology is the study of the flow and deformation of materials.[36] Often, a sample is loaded into a mechanical rheometer equipped with a cone and plate or parallel plate measurement geometry. The upper or lower plate can be moved to deform the sample, and the fluid response is detected. Through rheological investigation, the mechanical response of materials can be optimized in new technologies.

In creep tests, a constant stress (σ_i) is applied to a sample and the displacement in terms of strain (γ) is measured, where γ is the displacement of the moving plate. The creep compliance is calculated from γ as $J(t) = \gamma(t)/ \sigma_i$. In creep tests, elastic materials have a small, time-invariant

creep, and viscous fluids have a linear creep response. In yield stress fluids, microstructure persists at low stresses but is degraded at shear rates above the yield stress (σ_0). The yield stress can be characterized by comparing J(t) at stresses above and below σ_0. Below σ_0, J(t, σ_i) has a small, time-invariant creep. Above (σ_0), J(t, σ_i) will increase linearly.

The steady-state response of complex fluids can be probed through the application of linear or oscillating deformations. In response to deformation, the establishment of steady-state microstructure may not be instant and often occurs at times on the order of milliseconds to minutes in complex fluids.[36] In steady shear rheology, the viscosity as a function of shear rate is measured at steady-state. For Newtonian fluids, the viscosity is not dependent on the magnitude of the applied deformation. In complex fluids, the viscosity is often shear rate dependent. Shear-thinning, characterized by a decrease in viscosity with applied shear rate, is common in complex fluids; the applied deformation results in the degradation or orientation of microstructure.

In frequency-dependent rheology an oscillating shear deformation of frequency (ω) is applied to a sample and the response is measured at steady-state. The complex shear modulus (G*) relates the applied oscillating strain to the resulting stress as $\sigma(t) = G^*\gamma(t)$. The real and imaginary components of G* are the storage modulus (G') and the loss modulus (G"). The storage modulus is a measure of deformation energy stored in the system and represents the elasticity; the loss modulus is a measure of the energy used in the deformation process and represents the viscous behavior of the system.[37] The loss factor (tanδ) is the ratio of the viscous and elastic portions of deformation, where tanδ = G"/G'. It follows that fluids of tanδ > 1 are liquid-like and tanδ < 1 are solid-like.[37]

1.4 Introduction to Dynamic Light Scattering

The properties of a material on the nanometer or micron length scale are critical to the macroscopic properties characterized by rheology. The characteristic time (τ_c) of the system can be extracted from microdynamical characterization by DLS. To perform a DLS experiment, a laser enters a transparent sample, and is partially scattered by particles, polymers or microstructural features present in the sample. The rate of decorrelation of scattered light is related to the size of scatters in a sample. DLS has been used probe the microdynamics of chitosan solutions.[9,38,39]

The length scale probed (l) by DLS is set by the scattering vector (q) as $l = 2\pi/q$. The scattering vector can be controlled by the selected scattering angle (θ), laser wavelength (λ), and the refractive index of the solvent (n), as in Eqn. 1.3.1:[40]

$$q = \frac{4\pi n}{\lambda}\sin\left(\frac{\theta}{2}\right) \qquad \text{Eqn. 1.3.1}$$

The normalized intensity autocorrelation function $g_2(q, \tau)$ is computed by the instrument correlator from fluctuations in the measured intensity of light measured at the detector. The length scale of these fluctuations depends on the size of the scatters; large scatters diffuse more slowly, and, thus, their position in a solution will also change more slowly, leading to longer fluctuations. Quantitatively, $g_2(q, \tau)$ is calculated using Eqn. 1.3.2:

$$g_2(q,\tau) = \frac{\langle I_T(q,\tau) I_T(q,0)\rangle}{\langle I(q,\tau)\rangle_T^2} \qquad \text{Eqn. 1.3.2}$$

For most solutions, the dynamic structure factor $f(q,\tau)$ is related to $g_2(\tau)$ through the Seigert relation where β is the coherence factor, as shown in Eqn. 1.3.3. The value of the coherence factor can be found from the zero τ limit of $g_2(q,\tau)$.

$$g_2(q,\tau) = 1 + \beta|f(q,\tau)|^2 \qquad \text{Eqn. 1.3.3}$$

In gels and other non-ergodic systems, the ensemble averaged intensity (I_E) is dissimilar to the time averaged intensity. In these systems, the measured intensity will vary as the sample is moved; different microenvironments have different characteristic I_E values. In these cases, Eqn. 1.3.3 is not valid as variations in the ensemble averaged intensity must also be considered. A treatment proposed by Pusey and van Megen for non-ergodic systems can be used to determine $f(q,\tau)$ by modeling the scattering dynamics as random displacements about a fixed point, shown in Eqn. 1.3.4.[41]

$$f(q,\tau) = 1 + (I_T/I_E)\{[g_2(q,\tau) - \beta + 1]^{1/2} - 1\} \qquad \text{Eqn. 1.3.4}$$

Differently sized particle populations in a dilute solution of colloids, vibrations in gels or networks, and microstructural features of disparate length scales may result in multiple relaxation times. By fitting $f(q,\tau)$ as an exponential decay with m relaxation modes, τ_c of each mode may be extracted using Eqn. 1.3.5.

$$f(q,\tau) = \sum_{i=1}^{m} A_i(q)\exp(-\tau/\tau_{c,i}) \qquad \text{Eqn. 1.3.5}$$

1.5 Shear banding and flow characterization

Complex fluids have the mechanical properties of an ideal Hookean elastic solid and a Newtonian viscous fluid due to microstructural features; examples of complex fluids include polymer solutions, gels, soft glassy materials, and pastes.[42] Often, the characteristic length scale of complex fluids is mesoscopic, ranging from the molecular to that of the flow.[43] By altering the microstructure, complex fluids can be tailored for use in a variety of applications. For instance, paint spreads easily when applied but will not run, as a result of colloidal microstructure underlying shear-thinning rheological behavior. Other examples of functional complex fluids include shaving cream, lotion, mayonnaise, and biological solutions such as blood and mucus.

The flow of complex fluids is often non-linear in response to the application of a macroscopically homogenous shear rate.[43] In shear banded flows, bands of distinct shear rates and viscosities coexist within the sheared sample. A gradual change in shear rates, known as shear rate inhomogenitiy,[44] is also possible. Studying shear banding is important as it may interfere with the interpretation of bulk rheological data. Also, shear banding may affect the processing of complex fluids industrially. Regions of high viscosity may not mix completely, leading to, for instance, inconsistencies in a product.

1.5.1 Shear banding in yield stress fluids

In shear banding fluids, the underlying constitutive relationship can yield a non-monotonic flow curve in which the measured shear rate is predicted to decrease over a range of shear stresses. Because a decrease in stress with shear rate is unstable, the flow splits into

domains of high and low shear rates. Overall, a stress plateau is observed, as is the case in our chitosan solutions.[45] Shear banding can occur at steady-state or transiently.

Broadly, there are two types of yield stress fluids: thixotropic and simple (non-thixotropic). In thixotropic yield stress fluids, the microstructure and flow are strongly coupled. Flow induces microstructural breakup while Brownian motion induces regrowth, processes known as shear rejuvenation and aging. In these systems, shear banding dynamics depend strongly on the intrinsic time scale of material restructuring.[46]

In simple, non-thixotropic yield stress fluids the flow curve is not necessarily non-monotonic. Examples of simple yield stress fluids include microgels, dense emulsions, and foams.[45] The rheological characterization of chitosan solutions is indicative of non-thixotropic flow, as the measured flow curve is not affected by flow direction and shear history. The transmission of force in a complex fluid may be localized resulting in stress heterogeneity, a disparity between the local and average stresses.[47] Stress heterogeneity can lead to shear banding if the local shear stress falls below the yield stress.[48] In the simplest case, an un-yielded band of fluid with $\dot{\gamma} = 0$ coexists with a yielded band of $\dot{\gamma} > 0$.

Distinct bands as well as highly curved velocity profiles have been observed in solutions of concentrated xanthan gum, a highly charged polysaccharide.[49] Shear banding in polysaccharide solutions, including chitosan, has largely been unexamined.

1.5.2 Flow characterization techniques

A variety of experimental techniques have been used to evaluate shear banding in complex fluids including nuclear magnetic resonance (NMR) microscopy, DLS, ultrasound velocimetry (USV), and time-resolved particle image velocimetry (PIV).[50] By tuning magnetic field gradient pulses and resonant radiofrequency pulses, the translational displacement over a fixed time interval can be extracted using NMR microscopy.[51] DLS in homodyne mode or heterodyne mode can be used to extract local velocities.[50] In homodyne mode, the shear rate can be extracted from the characteristic decay time.[50] In heterodyne mode the scattered light is mixed with a reference beam, and the velocity can be extracted from the resulting oscillations.[50] In USV, an ultrasonic signal is scattered by fluid microstructure or tracers; the velocity can be extracted from cross-correlation.[52]

In PIV, the position of tracer particles is cross-correlated to extract the local velocity. PIV is limited to transparent samples and requires significant seeding with tracers. In comparison to other techniques, PIV has superior temporal and spatial resolution.[50] We employ a PIV methodology developed for one-dimensional shear flow in Wei et al.[44] Inherent to this methodology is the assumption of zero velocity components perpendicular to the gap.

1.6 Active motion of colloids

1.6.1 Colloids and Brownian motion

Colloids are solid particles with diameters of 1 nm to 10 μm suspended in liquid media.[53] Colloidal shape may range from the ubiquitous sphere to rods, cuboids,[54] peanut,[55] and other exotic shapes[56] enabling entropic self-assembly.[57] Additionally, colloids may be monophasic or biphasic as in the case of Janus, patchy, core-shell, or lock-and-key colloids.[56] Surface

modification enables additional application-specific control to alter charge, hydrophobicity, or add large functional components like polymers, proteins, or DNA.[58] The great diversity in the field of colloids may enable new technologies in the detection and treatment of cancer,[59] catalysis,[60] optics,[60] electronics,[60] magnetics,[60] batteries[61] and more.

In dilute solutions on the microscopic scale, the motion of colloids can be understood through competing viscous frictional forces and Brownian motion. Brownian motion is random motion from the bombardment of the colloid by surrounding molecules and results in particle diffusion. For a spherical particle, the Stokes-Einstein equation (Eqn. 1.5.1) describes the diffusion coefficient (D_0) in terms of the particle radius (R), thermal energy (ΔE_t) where $\Delta E_t = k_b T$ and k_b is Boltzmann's constant and T is temperature, and solvent viscosity (η_s):[53]

$$D_0 = \frac{k_B T}{6\pi\eta_s R} \qquad \text{Eqn. 1.5.1}$$

The resultant mean-squared displacement (ΔL^2) with time (τ) from the diffusion of spherical Brownian particles can be fully described in terms of D_0 and dimensionality (n) in Eqn. 1.5.2:

$$\Delta L^2 = 2nD_o\tau \qquad \text{Eqn. 1.5.2}$$

1.6.2 Introduction to active motion

The motion of passive particles on the micron length scale is controlled by Brownian randomizations and viscous drag with negligible inertial contributions.[62] In fact, in the regime of

colloidal motion viscous forces are ~10^4 stronger than inertial forces.[62] Consequently, applied motile forces are quite easily damped by viscous drag. In the case of autonomous propulsion, the particle is modified to harvest energy for supra-diffusive motion. For example, the flagella on bacteria enable swimming by providing a mechanical power source.[63]

Active motion has been generated synthetically using asymmetric chemical reactivity to generate chemical energy through self-diffusiophoresis.[64] In the case of platinum Janus particles, hydrogen peroxide fuel decomposes into oxygen at the platinum surface as shown in Eqn. 1.5.3:

$$2H_2O_2 \xrightarrow{Pt} H_2O + O_2 \qquad 1.5.3$$

In the micro-environment of the particle, the concentration of hydrogen peroxide will be highly uneven resulting in an inhomogeneous pressure field that drives fluid flow locally at the surface of the particle.[64]

The hydrogen peroxide-platinum modality of self-diffusiophoresis has been well studied.[11,12,65,66] However, the need for hydrogen peroxide fuel and the generation of oxygen may be problematic in application, including the human body. Alternative systems have been developed including a silica-Iridium Janus particle with hydrazine chemical fuel.[67] Similarly, Ma et al. has successfully fabricated active, biocompatible Janus particles of hollow mesoporous silica and three different enzyme coatings.[68]

Active motion can also be induced by the application of external directing fields, although debate around the classification of this motion as truly active exists due to the incomplete autonomy of these systems.[8] Indeed, the compulsory application of an external field may in itself be problematic or expensive. However, the inherit limitations of chemical self-diffusiophoresis, for instance, are not limitations in directed assembly. For instance, the application of a strong magnetic field can constrain the orientation of magnetic Janus particles and prevent Brownian rotation to in effect direct particle motion.[69] Other examples of field induced active motion include the manipulation of metallic micro-rods using ultrasonic standing waves[70] and propulsion of metallodielectic Janus spheres under low frequency electric fields.[71]

The motion of active particles is dependent on the translational diffusion coefficient (c.f. Eqn. 1.5.1) and also the rotational diffusion coefficient (D_r), shown in Eqn. 1.3.4:

$$D_r = \frac{k_B T}{8\pi\eta R^3} \qquad \text{Eqn. 1.5.4}$$

The time scale of rotational diffusion (τ_R) is extracted from D_r as shown in Eqn. 1.5.5:[72]

$$\tau_{R=\frac{1}{(n-1)D_r}} \qquad \text{Eqn. 1.5.5}$$

The time scale of rotational diffusion is the relaxation time of correlated particle orientation. For a particle moving with propulsive velocity (v*), the persistence length (L) characterizes the distance moved by a particle in a single direction as $L = v^*\tau_R$.[72]

The relative importance of diffusion and rotation compared with active motion is quantified as the active Peclet number (Pe) and the persistence number (Pe_r).[72] The active Peclet number compares the time scale of diffusive to active motion, shown in Eqn. 1.5.6:

$$Pe = \frac{2RV}{D} \qquad \text{Eqn. 1.5.6}$$

The persistence number compares the length of ballistic motion from activity to the size of the particle, shown in Eqn. 1.5.7:

$$Pe_r = \frac{L}{2R} \qquad \text{Eqn. 1.5.7}$$

For Pe >> 1 and Pe_r >> 1 active motion is significant and Brownian contributions are negligible. For active colloids typical reported Pe numbers vary from 1-100.[72] For an idealized active colloid system of R = 0.25 μm and R = 0.5 μm, for active motion to be predominate over Brownian motion (Pe > 1) v* must exceed 0.45 μm/s and 1.8 μm/s respectively, following Eqn. 1.5.6.

1.6.3 Characterization techniques for active motion

Active motion has been characterized extensively using microscopy.[11–13,65,68,73–75] In this methodology, videos of particles moving across a coverslip are collected and an image processing software is used to obtain particle trajectories, from which ΔL^2 is extracted. The motion of particles is constrained to two dimensions (n = 2) and, thus, the extracted ΔL^2 is two-

dimensional. At short times relative to τ_R ($\tau << \tau_R$), v* can be extracted ΔL^2 by fitting data to a simple polynomial as shown in Eqn. 1.5.7:

$$\Delta L^2 = 2nD\tau + v^{*2}\tau^2 \qquad \text{Eqn. 1.5.7}$$

Theoretically, the two dimensional ΔL^2 should be related to the three-dimensional ΔL^2 by a factor of 3/2 following Eqn. 1.5.2. However, anisotropy may lead to discrepancies in ΔL^2 as well as v* obtained from two-dimensional and three-dimensional measurements.[76] Anisotropy is a common feature of active particles, as detailed in section 1.5.1. A small percentage of potential technologies may utilize two-dimensional motion of active particles across a surface as in the case of electronic circuit repair.[5] However, environmental remediation and biological applications will require three-dimensional characterizations. Thus, the development of accurate technologies to measure the three-dimensional ΔL^2 of active particles is an important part of successful development.

The dynamic structure factor, extractable from DLS measurements, is related to the three-dimensional ΔL^2, shown in Eqn. 1.5.8 for passive colloids:

$$f(q,\tau) = \exp(-q^2\Delta L^2/6) \qquad \text{Eqn. 1.5.8}$$

The three-dimensional ΔL^2 is the core piece of information contained in f(q, τ), as particles move in three-dimensions within the scattering volume. The length scale probed by DLS (l) is on the order of a micron, where $l = 2\pi/q$. The assumption of quadratic q-dependence

has not been validated in active systems. The direct extraction of ΔL^2 from f(q, τ), however, is not necessary to extract V. The propulsive velocity has been extracted from f(q, τ) directly in systems of motile bacteria[77,78] and spermatozoa.[79]

Chapter 2

Yield Stress and Rheology of a Self-Associating chitosan solution

2.1 Publication Information

Gasbarro, N. M., Solomon M. J. *Yield stress and rheology of a self-associating chitosan solution.* Rheological Acta, 2019. 58(11-12): 729-739.

Modifications have been made to the published document to adapt the content to this text.

2.2 Abstract

We report that aqueous solutions of high molecular weight chitosan display a regime of shear thinning at low shear rates that is consistent with the existence of an apparent yield stress. The concentration-dependent scaling of the apparent yield stress, $\sigma_0(c) \sim c^{2.8\pm0.2}$ in the concentration range c = 7.50 – 65.0 mg/mL, is consistent with a solution microstructure of fractal clusters. Dynamic light scattering measurements at high concentration indicate extremely slow microdynamics, consistent with the presence of a structured network or glassy fluid. At shear rates above yielding, a constant viscosity plateau was observed with concentration-dependent scaling below the gel point consistent with existing models of entangled and associating polymers. The addition of urea, a hydrogen bond and hydrophobic interaction disrupter, did not change the reported concentration-dependent scaling of the apparent yield stress or the plateau viscosity but did weaken the apparent yield stress magnitude by ~ 30% on average.

2.3 Introduction

Chitosan is a de-acetylated derivative of the naturally occurring biopolymer chitin. Chitosan is a copolymer of β-(1→4)-linked D-glucosamine ($C_6H_{13}NO_5$) and N-acetyl-D-glucosamine ($C_8H_{15}NO_6$); the fraction and distribution of acetylated groups varies. Unlike chitin, chitosan is soluble under mild acidic solutions (pH < 6.1)[14] due to the protonation of amino groups. Chitosan finds applications in multiple fields and industries; also, it is easily derivatized to tune its rheological properties for specific applications. Furthermore, it is biodegradable,[3] antimicrobial,[18,19] antifungal,[19,20] and hemostatic.[27] Chitosan exhibits low toxicity in the μg/mL range[4] and is used as a food additive.[21] Exogenous chitosan promotes ordered tissue reconstruction[80] and is a commercially available wound healing agent.[81] Chitosan derivatives are incorporated into cosmetics and consumer goods formulations.[22,23] There is potential for applications of chitosan in drug delivey,[24] wastewater treatment,[25] bio-fabrication,[26] and tissue engineering.[1]

Chitosan has been characterized by a variety of methods including rheology, urea addition as a probe of hydrophobic and hydrogen bonding interactions, and dynamic light scattering (DLS). The shear-rate dependent steady viscosity of chitosan solutions has been reported to display a low-rate plateau and a single regime of shear thinning, extending from low to high shear rates at high chitosan concentrations;[82–87] this behavior is typical of polysaccharides.[88] The reported scaling of the plateau viscosity (η_0) with concentration (c) for chitosan solutions follows $\eta_0 \sim c^m$; in the dilute regime m = 1.1-1.2[85,86] and in the semi-dilute entangled regime m = 3.3-5.2.[82,85,86] Shear thinning at low shear rates has been reported in chitosan-*graft*-polyacrylamide.[87]

Urea is used in polymer systems to disrupt hydrogen bonding and hydrophobic interactions, because it is believed to directly bond with polar groups and indirectly lower the penalty for solvent exposure to nonpolar groups. In the case of polysaccharide intercellular adhesion (PIA), a bacterially synthesized polysaccharide composed of D-glucosamine and N-acetyl-D-glucosamine monomers, urea addition significantly lowers the scaling of the concentration dependence of the solution viscosity.[89] The addition of urea to chitosan-β-glycerophosphate systems has been shown to hinder gelation.[90] Interestingly, chitosan aggregate formation[91] and chitosan polymer stiffness[92,93] are reportedly only marginally affected by urea addition while others report improved chitosan solubility upon urea addition.[94]

The microdynamics of chitosan in solution have been characterized using DLS. The intensity autocorrelation function derived from DLS is a single[39] or biphasic[9,38,39] exponential decay to an ergodic baseline, depending on the range of chitosan concentration studied. In semi-dilute solutions of chitosan, large associating structures have been inferred from DLS.[9,38,39] In the semi-dilute regime, the intensity autocorrelation function measured by DLS for chitosan solutions exhibits two relaxation times.[9,38,39] The dynamics of the slow relaxation process become increasingly retarded as concentration increases;[38,39] reports for the q-dependent power law scaling of the slower DLS decay time vary from 2.0 -2.8[38,39] (depending on chitosan concentration) and feature a stretched exponential for the slow relaxation process,[38] suggestive of non-diffusive behavior. At high chitosan solution concentrations, chitosan forms physical gels.[82] Physical gels are amorphous solids formed by the physical arrest of polymer dynamics, akin to the slow dynamics observed in glassy polymers, but in this case generated by associations and

other physical interactions.[95] Although chemically cross-linked chitosan gels have been studied using DLS,[96] to our knowledge such measurements have not been performed for physical gels of chitosan.

Corroborating findings from DLS, aggregates in chitosan solutions have been imaged by external wet-STEM,[10] TEM[9,10,16] and SEM.[10,17] In fact, TEM micrographs of dilute chitosan show a dense core and a loose shell with dangling chains[9] that become increasingly interconnected as concentration increases.[10] Contradictorily, chitosan aggregates are reportedly hydrophobic in nature but are only partially disrupted by urea[16,91] and form in fully deacetylated chitosan.[16] Microcrystalline domains of glucosamine have been hypothesized to underlie chitosan aggregation, but direct observation of glucosamine crystallinity has been limited to chitosan powders.[15] Thus, the nature of these aggregates remains unresolved.

Despite this prior characterization of the complex microstructure of quiescent chitosan solutions, there is a gap in the understanding of chitosan rheology. Specifically, the steady-state rheological behavior at low shear rates is unexplored. This low shear-rate regime is of fundamental interest because the low shear stresses potentially couple to weak or transient microstructures. The effect of this microstructure in flow is also relevant to the use of chitosan solutions for rheological control in a variety of product applications. For example, formulations of chitosan and cellulose nanofibers are injectable but subsequently gel at body temperature, enabling potential use in intervertebral disc tissue engineering.[97] Further, chitosan already is used to enhance the viscosity of food products[21] and cosmetics[23] as a natural, environmentally friendly thickener.

In this study, we probe the steady-shear flow curves of chitosan with a focus on the behavior of the apparent yield stress over a broad range of concentrations. Creep experiments further characterize the yield stress. Measurements of linear viscoelasticity are used to establish conditions of gelation. The role of physiochemical interactions is assessed by the addition of urea. These rheological behaviors are examined in light of accompanying measurements of solution microdynamics, as characterized by dynamic light scattering. Measuring both the microdynamics and rheology of these solutions allows analysis of the relationship between the two. Our hypothesis is that chitosan microstructure as inferred from the literature leads to the existence of an apparent yield stress.

2.4 Experimental Methods

2.4.1 Materials

High molecular weight chitosan from Hope Medical Chitosan GmbH (Halle (Saale), Germany) was used as received. The fraction of de-acetylation is 72%, from triplicate CHN elemental analysis by Elemental Analysis, Inc. (Lexington, KY) as in dos Santos et al.[98] The weight averaged molecular weight (M_W) was $8.2 \pm 0.4 \times 10^5$ g/mol from static light scattering (SLS) using a Zimm plot analysis (with compact goniometer system CGS-3, ALV GmbH, Langen, Germany) of four dilute concentrations (c.f. Figure 2.1).

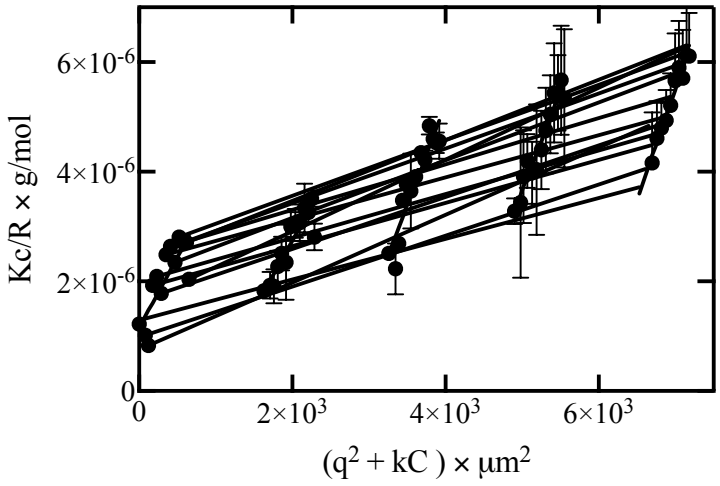

Figure 2.1 c_e determination from M_W measured from static light scattering (SLS). Zimm plot determination of the weight averaged molar mass (M_W) of the chitosan used in this study. The plot ordinate, Kc/R, is a characteristic quantity computed in static light scattering of polymer solutions; in the limit of low scattering angle and low concentration is it equal to the inverse of the M_W. The abscissa is a scaled coordinate that combines the polymer concentration, c, and the scattering vector, q, which depends on the scattering angle. A value of k = 16,323 $mLmg^{-1}\mu m^{-2}$ was selected to optimize data presentation in the above Zimm plot. The average Kc/R for two replicates of chitosan of c = 0.1, 0.2, 0.3 and 0.4 mg/mL in 0.3 M acetic acid and 0.15 M sodium acetate at T = 25° is reported at 12 angles from 30-150° (ALV/CGS-3, ALV Gmbh, Germany). Two data points with anomalous Kc/R values (likely because of dust contamination) were discarded. Values of Kc/R for limiting conditions $q^2 = 0$ and c = 0 were extrapolated from horizontal and vertical fits determined from weighted least squares regression. The molecular weight (M_W) from this analysis was $M_W = 8.2 \pm 0.4 \times 10^5$ g/mol, and the radius of gyration (R_g) was R_g = 71 nm. The hydrodynamic radius (R_h) was estimated from the reported ratios of $R_g/R_h = 2.3 – 2.5$ for chitosan and found to be R_h ~30 nm. (Berth et al. *Progr. Colloid Polym. Sci.*, 2002, 119, 50-57).

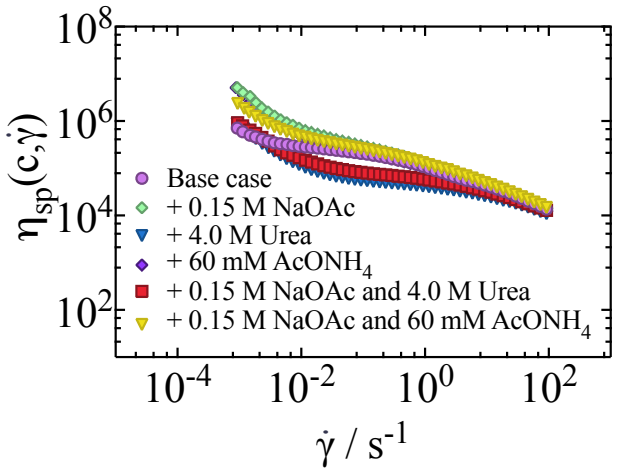

Figure 2.2 Effect of solvent selection on solution viscosity.
To determine the effect of solvent on $\eta_{sp}(c,\dot{\gamma})$, two additives and a salt were added to chitosan solutions of c = 40 mg/mL in addition to the base case solvent of 0.3 M acetic acid (AcOH). The solvent viscosity was independently measured using Ubbelohde viscometry. The two additives, 4.0 M urea and 60 mM ammonium acetate ($AcONH_4$), were selected for their ability to disrupt hydrophobic interactions and/or hydrogen bonds, and a high concentration of 0.15 M sodium acetate (NaOAc) was added to probe hydrophobic effects. For all measurements, data were collected using a 1° cone and plate geometry with d = 60 mm at T = 25° (AR-G2, TA Instruments). Preceding steady shear viscosity measurement, samples were pre-shared at σ = 14.1 Pa for two minutes followed by a five minute wait period. The value of $\eta_{sp}(c,\dot{\gamma})$ from one run for each solvent permutation is reported as measured in an increasing direction. The addition of NaOAc and $AcONH_4$ did not affect $\eta_{sp}(c,\dot{\gamma})$, and urea lowered the plateau viscosity $\eta_{sp,1}$ as expected. Thus, the qualitative functional form of $\eta_{sp}(c,\dot{\gamma})$ was not significantly affected by solvent variation; a mid-shear rate viscosity plateau and two shear thinning regions are apparent at high and low shear rates in all cases.

Solutions were prepared using HPLC-grade water, 0.3 M acetic acid, and 0.15 M sodium acetate. Urea was included in some solutions at a concentration of 4.0 M. The excess salt concentration was used to minimize the polyelectrolytic contribution of de-acetylated groups; however, solvent selection had a minimal impact on solution properties (c.f. Figure 2.2). For DLS and SLS work, the solvent was triple filtered (pore size = 0.02 μm, Whatman Anatop). After mixing, samples were rolled at 0.9 rpm for 1-3 weeks at room temperature until the polymer was completely dissolved, as indicated by visual inspection.

2.4.2 Mechanical Rheometry

The effect of concentration and additives on the steady-shear viscosity of chitosan solutions was measured with a controlled stress AR-G2 rheometer equipped with a 60 mm, 1° stainless steel cone and plate fixture at T = 25 °C (AR-G2, TA Instruments). A solvent trap was used to minimize sample evaporation. Replications were performed at each condition until the relative standard error was less than 0.20; the number of replications varied from two to five per condition. The possibility of slip or flow instability as confounders of results was evaluated by comparing results in fixtures of three different cone angles: 0.5°, 1.0° and 2.0°. The geometry independence of the viscosity in different cone angles and effective gap heights is a strong indication of slip-free flow.[99] Results were independent of fixture over the full range of shear rate and shear stress conditions studied (c.f. Figure 2.3). Because of the possibility of aging and/or thixotropic rheology, preliminary tests were performed to determine pre-shear (c.f. Figure 2.4) and wait time (c.f. Figure 2.5) conditions for all specimens. For all rheological experiments a pre-shear episode of shear stress $\sigma = 14.1$ Pa was applied for two minutes; a wait time of five minutes was then applied.

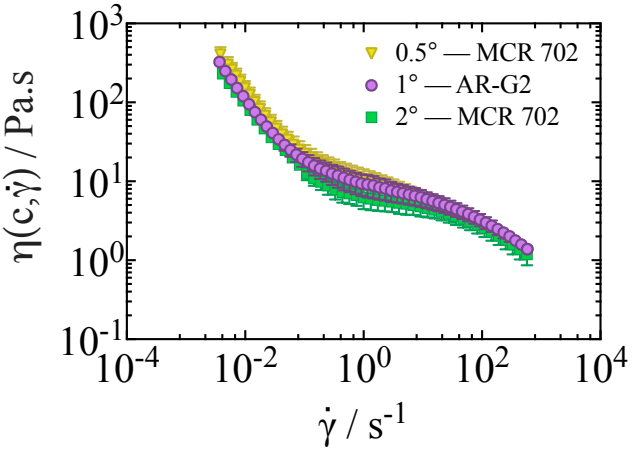

Figure 2.3 Assessment of potential wall slip and instrumental variability. Samples of c = 40 mg/mL chitosan in 0.3 M acetic acid and 0.15 M sodium acetate were pre-treated at σ = 14.1 Pa for two minutes followed by a five minute equilibration. The angle of the cone and plate as well as the rheometer used are indicated in the legend. Steady shear viscosity measurements with the 0.5° and 2° cone and plate on the MCR 702 were made from $\dot{\gamma}$ = 0.001 - 1000 s^{-1} operating in the constant strain mode (Anton Paar). Steady shear viscosity measurements with the 1° cone and plate geometry were taken on the AR-G2 (TA Instruments); measurements were made from $\dot{\gamma}$ =5.8x10^{-6} – 5.8x10^{2} s^{-1}. AR-G2 data above 0.001 s^{1} was reported to match the detection limit of the MCR 702. All data is the average of three runs and error bars show standard error. Data were collected at T = 25 °C. A hood was used to control sample evaporation. The measured values of η(c,$\dot{\gamma}$) are indistinguishable, consistent with the assumed no slip condition. No significant differences were observed between the instruments.

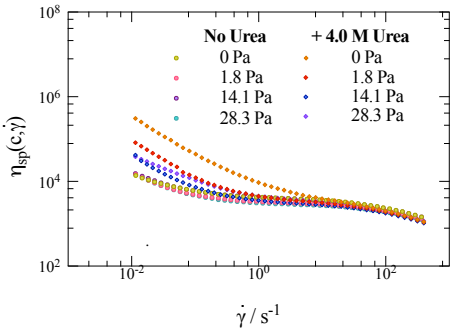

Figure 2.4 Pre-shear stress evaluation.

To determine the effect of pre-shear and select a standard pre-shear condition, the steady shear viscosity of 40 mg/mL chitosan in 0.3 M acetic acid and 0.15 M sodium acetate with and without 4.0 M added urea was collected after one of four shear stresses of σ = 0 Pa, 1.8 Pa, 14.1 Pa and 28.3 Pa was applied for two minutes and the sample was allowed to equilibrate for five minutes. The steady shear viscosity was measured at T = 25 °C using a 1° cone and plate geometry with d = 60 mm (AR-G2, TA Instruments). Variability was assessed through the $\dot{\gamma}$-averaged relative standard error (RSE) for all runs at a concentration, and variability was considered minimal if RSE < 0.2. The pre-shear condition had a minimal effect on the c = 40 mg/mL case without urea (RSE = 0.07). For c = 40 mg/mL with urea, a pre-shear condition of $\sigma > 0$ was necessary for low variability (RSE = 0.084). For this reason, a standard pre-shear condition of σ = 14.1 Pa was selected for use in all experiments.

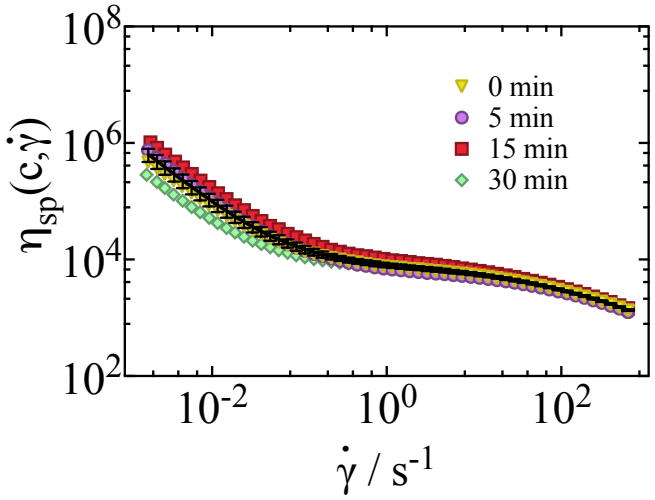

Figure 2.5 Equilibration/wait time evaluation.
To determine the effect of wait time on the measured flow curve, samples of 40 mg/mL chitosan in 0.3 M acetic acid and 0.15 M sodium acetate were sheared for two minutes at σ = 14.1 Pa followed by one of four wait times: 0, 5, 15 or 30 minutes. Measurements were done using a 1° cone and plate geometry with d = 60 mm at T = 25 °C (AR-G2, TA Instruments).
The average of $\eta_{sp}(c,\dot{\gamma})$ for all wait times with standard error bars for is shown in black. The $\eta_{sp}(c,\dot{\gamma})$ variation at low $\dot{\gamma}$ is not a monotonic function of wait time and variability was not significant as the $\dot{\gamma}$-averaged relative standard error (RSE) was minimal (RSE = 0.116). Therefore, a standard wait time of five minutes, which falls within the standard error of this set, was selected for use in all runs.

After the episodes of pre-shear and wait time, the steady-state viscosity was measured as a function of shear rate. The criterion for steady state was a change of less than 3% over four consecutive 15 s periods. In the low shear rate region, sample equilibration was extremely slow; for example, at $\dot{\gamma}$ = 0.0001 s^{-1} the equilibration time exceeds two hours. Slow equilibration at low shear rates in yield stress fluids can cause artificially low apparent viscosities; a spurious low shear rate viscosity plateau can be measured if the sampling time is shorter than the equilibration time.[48,100] Due to sample evaporation the sampling window could not be extended sufficiently to characterize steady-state behavior at such low shear rates; instead a maximum sampling time of 10 minutes per shear rate was used. With this sampling time, steady-state behavior was achieved for shear rates $\dot{\gamma}$ > 0.0017 s^{-1}. Due to low torque sensitivity at low shear rates, a secondary

minimum shear rate, determined using a set of silicone oil standards, was also applied if above the minimum shear rate for sample equilibration. Finally, the maximum shear rate for measurements was $\dot{\gamma} = 5.8\times10^{2}\ s^{-1}$ or determined by the condition at which the test fluid was expelled from the rheometer gap. Data were collected in the direction of low to high shear rate. The average collection time for a sweep was ~ 1.75 hours.

Oscillatory rheology experiments were performed with an MCR 702 TwinDrive Rheometer (Anton Paar) equipped with a smooth, 50 mm diameter, 0.5° cone and plate geometry. A solvent hood was used to control evaporation. After episodes of pre-shear and wait time, an angular frequency (ω) sweep of ten points per decade from $\omega = 3.96$ to $\omega = 326$ rad/s was performed for seven concentrations of chitosan ranging from c = 40 – 70 mg/mL with and without added 4.0 M urea in 0.3 M acetic acid and 0.15 M sodium acetate at a constant temperature of T = 25°C. The criterion for reaching steady state was a change of less than 0.05% over 4 s. Five replicates were performed at each condition.

To confirm the existence of the yield stress, creep experiments were performed with an MCR 702 TwinDrive Rheometer (Anton Paar) operating in constant strain mode equipped with a smooth, 50 mm 0.5° cone and plate geometry. A solvent hood was used to control evaporation. After episodes of pre-shear and wait time, constant stresses of σ_i = 1-10 Pa were applied for a period of t = 300 s followed by a relaxation period of t = 300 s of $\sigma_i = 0$ Pa. A solution with c = 65 mg/mL chitosan in 0.3 M acetic acid and 0.15 M sodium acetate aqueous solution at a constant temperature of T = 25°C was studied with five replicates of each applied stress condition.

2.4.3 Entanglement and gel point concentrations

To determine the entanglement concentration, the overlap concentration of the chitosan material was first measured by Ubbelohde viscometry both with and without 4.0 M added urea. The kinematic viscosity (ν) of chitosan solutions of c < 10.0 mg/mL was measured at T = 25°C in Ubbelohde viscometers of capillary inner diameter chosen from $Ø_i$ = 0.36, 0.46, 0.58, 0.78, and 1.03 mm (SI Analytics GmbH, Mainz, Germany) with an AVS 350 Automatic Viscosity System (SI Analytics GmbH, Mainz, Germany). Before measurements were collected, the Ubbelohde viscometer was equilibrated in the bath for ten minutes and an unrecorded run was performed to wet the capillary. For each experiment, seven consecutive measurements were performed. The average drop time was corrected for kinetic energy effects. At each concentration and solvent condition, two sets of experiments were done using different solutions, and the average of both sets is reported. The viscosity (η) is related to ν by $\eta = \nu\rho$, where ρ is the solution density (ρ = 1.005 mg/mL and ρ = 1.065 mg/mL for the solutions with added 4.0 M urea). As discussed further in SI.6, the Ubbelohde measurements are not in a low-shear limit, because of the shear-sensitivity of the chitosan solutions, even at the low concentrations selected for Ubbelohde viscometry. Instead, they are in the mid-plateau region. As discussed subsequently, the mid-shear plateau region is determined by the molecular properties of the polymer; the low-shear regions are governed by microstructure. The intrinsic viscosity from the mid-shear rate region accessed by Ubbelohde viscometry represents the molecular properties of the polymer. The intrinsic viscosity $[\eta]_0$ is determined to be 0.58 mL/mg – both with and without urea; in both cases the critical overlap concentration is estimated to be c* = 1.7 mg/mL from this value of the intrinsic viscosity (details also in SI.6).

The entanglement concentration (c_e) was determined using the relation $c_e = c^* n_e^{(3\nu-1)}$ [101] where n_e is the entanglement to monomer molecular weight ratio and ν is the excluded volume exponent. The entanglement to monomer molecular weight ratio of chitosan ($n_e = 8$) is insensitive to chitosan degree of deacetylation and molecular weight.[102] The excluded volume exponent of chitosan ($\nu = 0.55$) is also reportedly insensitive to chitosan degree of deacetylation and molecular weight and also to ionic strength.[103] Further, the conformation of high molecular weight chitosan in dilute solution is not affected by the addition of 4.0 M urea as assessed through the Mark-Houwink exponent[27] or through the intrinsic viscosity of the chitosan (c.f. SI.6). Due to the reported insensitivity of n_e, ν and $[\eta]_0$, a single value of $c_e = 7$ mg/mL is used both with and without 4.0 M urea.

The gel point concentration was determined by small-amplitude oscillatory shear measurements of the linear viscoelastic moduli. The storage and loss moduli, G'(ω) and G"(ω), were measured for seven concentrations of chitosan from c = 40 – 70 mg/mL without and with 4.0 M urea (c.f. Figure 2.6). The loss factor tan(δ) = G"(ω)/G'(ω) was measured for each condition. Briefly, the gel point is taken as the concentration at which G' = G" (i.e. tan(δ) = 1) and at which the power law scaling of the two moduli is the same, as in ref. [104] and as adapted from Winter and Chambon.[105] Low frequencies were excluded from the analysis due to the apparent G'(ω) plateau that has been associated with both weak network structures and instrument effects.[106] Using linear interpolation, the gel point without urea is $c_g = 47$ mg/mL and with urea is $c_{g+U} = 55$ mg/mL (c.f. Figure 2.7).

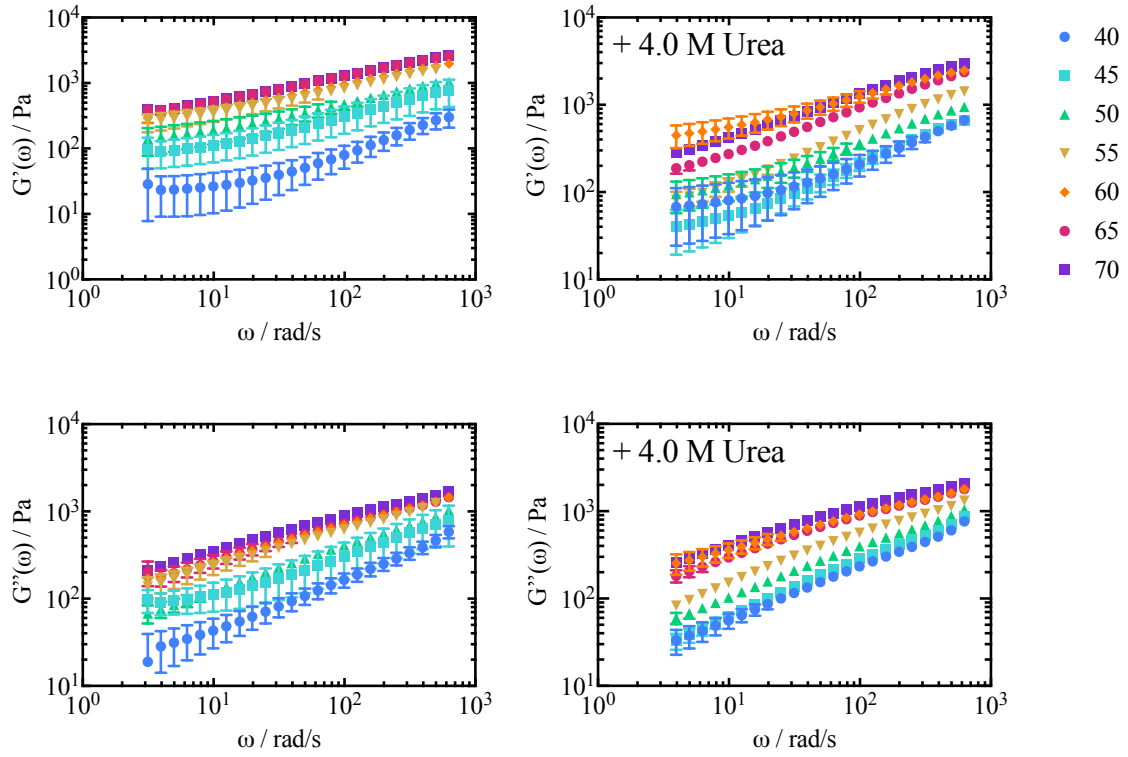

Figure 2.6 Storage and Loss moduli for chitosan solutions.
The average storage and loss moduli, G'(ω) and G"(ω), for chitosan solutions was measured using oscillatory rheology as detailed in the Methods section. Error bars represent standard error.

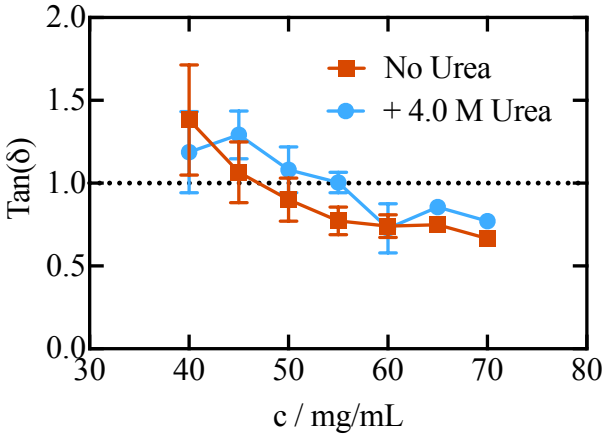

Figure 2.7 Tan(δ) of chitosan with and without urea.
Tan(δ) is plotted as a funciton of concentration without and with 4.0 M added urea. The error bars represent the standard error of the frequency averaged power law scaling region of G' and G" for each concentration. The dotted line at tan(δ) = 1 represents the transition from sol to gel. From linear extrapolation, the gel point without (c_g) and with 4.0 M added urea (c_{g+U}) were found to be c_g = 47 mg/mL and c_{g+U} = 55 mg/mL.

2.4.4 Dynamic Light Scattering (DLS)

DLS was performed using a compact goniometer system (CGS-3, ALV GmbH, Langen, Germany) with a multi-tau digital correlator (ALV/LSE-5004, ALV GmbH, Langen, Germany). For DLS, the minimum decay time of the correlator was 25 ns.

A laser with wavelength λ_0 = 632.8 nm (Model 1145P HeNe laser, JDSU, California) was used in the angular range of θ = 20-150°, which corresponds to a scattering vector (q) range of 4.59 $\mu m^{-1} < q < 25.5\ \mu m^{-1}$, where $q = 4\pi n \sin(\theta/2)/\lambda_0$; n is the refractive index of the solvent. Sample vials were pre-cleaned by sonication in HPLC grade ethanol-water solution and in triple filtered (d = 0.02 μm, Whatman Anatop) HPLC grade acetone solution. All measurements were done at T = 25.0 ± 0.5°C.

Chitosan solutions of c = 40 mg/mL and c = 65 mg/mL were studied as they are conditions at which yield stress behavior is observed in the entangled and gelation regimes, where previous DLS characterization of chitosan has been limited. Run times were 2.0 hours for c = 40 mg/mL and 4.0 hours for c = 65 mg/mL; these long durations were used to capture the slow dynamics of the solutions. For all concentrations, five measurements at nine angles were performed on three replicates, for a total of 15 runs per angle. A run was discarded if the variability parameter I_{dev} exceeded 4.5, as defined by $I_{dev} = I_{max}(q)/\langle I(q)\rangle_T$, where $I_{max}(q)$ is the maximum intensity recorded during a run and $\langle I(q)\rangle_T$ is the time averaged intensity. Using this criterion, the total number of runs per angle at a given concentration varied from 3 – 12 with a mean of 7. For both samples, the normalized intensity autocorrelation function, $g_2(q, \tau)$ =

$\langle I_T(q,\tau)I_T(q,0)\rangle/\langle I(q,\tau)\rangle_T^2$, was computed by the instrument correlator from fluctuations in the measured intensity of light. Measurements were truncated at long times to eliminate regions where $g_2(t)-1 < 0$ because of an insufficiently resolved baseline.

The dynamic structure factor, $f(q,\tau)$, a common measure of polymer dynamics, was obtained from $g_2(q, \tau)$. The method used to convert from $g_2(q, \tau)$ to $f(q, \tau)$ depended on the ergodicity of the system. For ergodic samples, the decorrelation of scattering is captured within the experimental duration; the time-averaged intensity of a speckle, I_T, is equivalent to the intensity averaged over an ensemble of speckles, I_E. In these cases, $g_2(q, \tau)$ is related to the dynamic structure factor $f(q,\tau)$ through the Seigert relation below (Eqn. 1) where β is the coherence factor:

$$g_2(q,\tau) = 1 + \beta|f(q,\tau)|^2 \qquad \text{Eqn. 1}$$

The value of $\beta = g_2(q,0)-1$ was determined by extrapolating $g_2(q,\tau)$ to $\tau = 0$ for $\tau < 600$ ms. Samples of c = 40 mg/mL were determined to be ergodic, and this method was used to derive $f(q, \tau)$ from $g_2(q,\tau)$.

In non-ergodic systems $I_T \neq I_E$ and the Siegert relation does not apply; polymers are localized and do not explore their configuration space in the measurement time. To obtain I_E, the sample was manually rotated during measurement for five, 20 s runs at each attenuator and angle setting as per the methods of Joosten et al.[107] The theory of Pusey and van Megen for non-ergodic systems determines $f(q,\tau)$ by modeling the scattering dynamics by random displacements about a fixed point:[41].

$$f(q,\tau) = 1 + (I_T/I_E)\{[g_2(q,\tau) - \beta + 1]^{1/2} - 1\} \qquad \text{Eqn.2}$$

For c = 65 mg/mL, non-ergodicity was confirmed by the observation that $I_T \neq I_E$ and Eqn. 2 was therefore used. Model fits to the measured $f(q,\tau)$, as discussed further in the Results, were performed using non-linear least squares fitting (implemented in MATLAB) with no weighting unless otherwise specified.

2.5 Results

2.5.1 Shear-dependent viscosity characterization

Figure 2.8 reports the concentration dependence of the shear-rate dependent viscosity for chitosan solutions of 3 mg/mL and 80 mg/mL. In Figure 2.9, select concentrations from Figure 2.8a and Figure 2.8b without and with 4.0 M added urea are directly compared. There are several characteristic features of these curves: (i) the degree of shear thinning in the chitosan solutions is large, extending more than two orders of magnitude in viscosity; (ii) in the entangled regime (c > ce) two distinct regions of shear thinning are apparent; and (iii) features of the data, including plateau viscosities and transition shear rates, shift systematically with concentration.

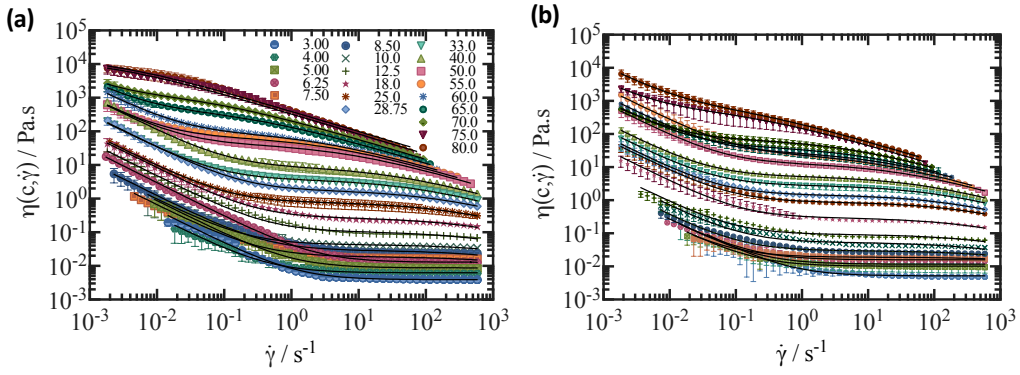

Figure 2.8 Chitosan steady Shear viscosity with and without added urea.
The steady shear viscosity of chitosan solutions in 0.3 M acetic acid and 0.15 M sodium acetate without (a) and with added 4.0 M urea. Data were collected as detailed in the Methods section of the paper. Selected concentrations are shown in Figure 2.9 in the main text of the paper.

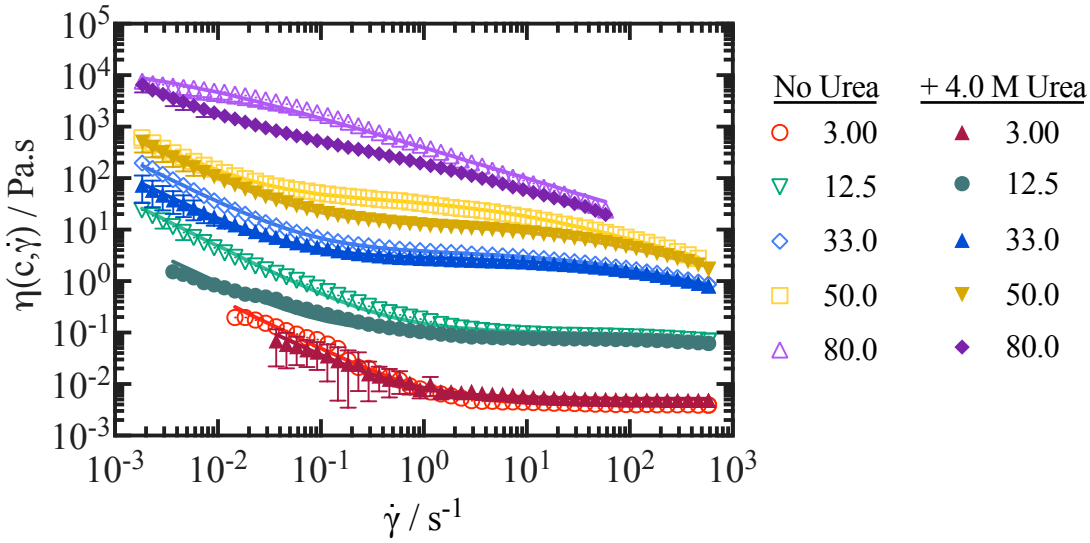

Figure 2.9 The shear rate dependent viscosity ($\eta(c,\dot{\gamma})$) of chitosan solutions of c = 3 – 80 mg/mL without and with 4.0 M added urea for select concentrations.
Lines show calculated viscosity fits based on Eqn. 3-4. The full dataset are available in Figure 2.8.

The complex functional form of the flow curve for these solutions was confirmed by a number of auxiliary tests. Specifically, solvent effects (c.f. Figure 2.2), instrumental errors (c.f. Figure 2.3), sensitivity of results to hysteresis (c.f. Figure 2.10), and slip (c.f. Figure 2.3) were

evaluated. In addition, we confirmed that this type of flow curve was not unique to the particular sample of high molecular weight chitosan (c.f. Figure 2.11).

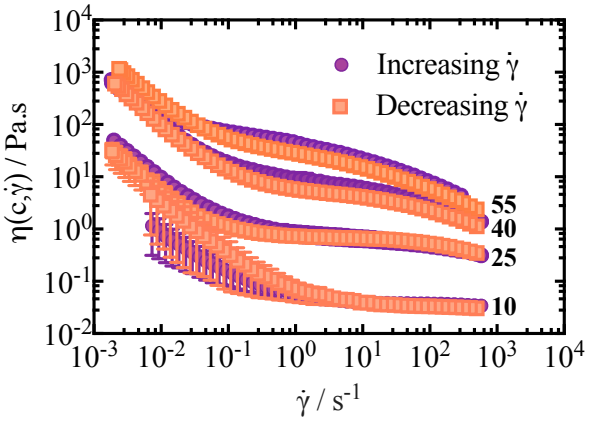

Figure 2.10 Hysteresis and flow direction.
Two sets of data were collected in the direction of increasing and decreasing shear rate at T = 25° C without urea in 0.3 M acetic acid and 0.15 sodium acetate. Both sets of data were collected after a pre-shear of σ = 14.1 Pa was applied for two minutes followed by a five five minute equilabration. The decreasing shear rate dataset was collected from $\dot{\gamma}$ = 500 – 0.002 s^{-1} for c = 10, 25, 40 and 55 mg/mL using an MCR-702 rheometer operating in constain strain mode with a 0.5° cone and plate geometry with d = 50 mm. The increasing shear rate data set was collected as indicated in the Methods section using an 1° cone and plate geometry with d = 60 mm (TA Instruments, AR-G2). There is no significant difference between the data sets; for $c > c_e$ there are two regions of shear thinning and a viscosity plateau, and for $c < c_e$ thee is one region of shear thinning and a viscosity plateau. From this, we conclude that shear history does not significantly effect the apparent steady shear viscosity.

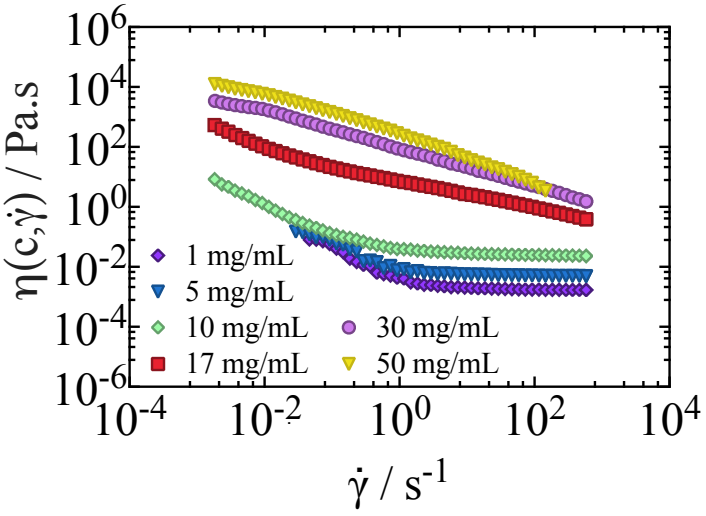

Figure 2.11 Effect of chitosan source.
Six chitosan solutions were made from a different speciment of chitosan than used in the main text, and as dissolved in 0.3 M acetic acid and 0.15 M sodium acetate. The chitosan used was purchased from Sigma Aldrich and has a molecular weight of 190-310 kDa and fraction of deactylation of 75-85% as reported by the manufacturer. Solutions were pre-sheared at σ = 14.1 Pa for two minutes followed by a five minute equilibration period; next, the steady shear viscosity $\eta(c, \dot{\gamma})$ was measured in the direction of increasing shear rate ($\dot{\gamma}$) using a 1° cone and plate geometry with d = 60 mm at T = 25 °C (AR-G2, TA Instruments). Results are qualitiatively consistent with the measurements reported in the main text, with a low-shear plateau stress, a mid-shear plateau viscosity, and high rate shear thinning regions.

In addition, to corroborate the existence of a yield stress in this chitosan system, Figure 2.12 shows the creep compliance $J(t, \sigma_i)$ upon application of a constant applied stress (σ_i) and subsequent relaxation ($\sigma_i = 0$) for the particular case of c = 65 mg/ml. The creep compliance was calculated from the measured strain ($\gamma(t)$) as $J(t) = \gamma(t)/\sigma_i$. $J(t, \sigma_i)$ reaches a constant value for σ_i = 2 – 5 Pa but increases linearly for $\sigma_i > 5$ Pa. The creep recovery for c = 65 mg/mL decreases with σ_i and is minimal at σ_i = 6 Pa and 10 Pa, indicating a loss of elasticity beyond ~ 6 Pa. The behavior for c = 65 mg/ml suggests that the yield stress is between 5 and 6 Pa for this material. That is, the material flows at an applied stress of 6 Pa (because of the linear increase in $J(t, \sigma_i)$ with time); such flow is not apparent at 5 Pa.

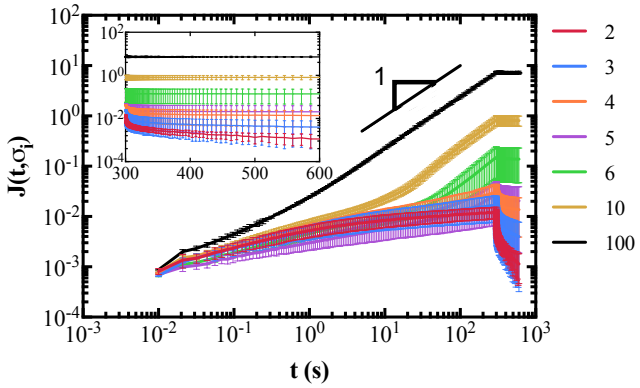

Figure 2.12 Measured shear creep compliance and creep recovery $J(c, \sigma_i)$.
Chitosan solutions at c = 65 mg/mL during a period of applied stress σi = 1 – 10 Pa (indicated in the legend) from t = 0 - 300s and subsequent relaxation at τ = 0 Pa from t = 300-600 s. The inset shows the relaxation period in greater detail. Error bars represent standard error of the mean.

2.5.2 Shear-dependent viscosity modeling

The Cross model is a commonly applied equation for the steady-shear rheology of shear-thinning polymers, including chitosan[85,108] and other polysaccharides.[109] To account for and model the viscous response at low shear rates, we add a yield stress term to a simplified form of the Cross model:

$$\eta(c,\dot{\gamma}) = \frac{\sigma_0(c)}{\dot{\gamma}} + \frac{\eta_1(c)}{1+(\lambda(c)\dot{\gamma})^m} \qquad \text{Eqn. 3}$$

Here, $\sigma_0(c)$ is the yield stress, m is the characteristic exponent, $\eta_1(c)$ is the plateau viscosity, and $\lambda(c)$ is the characteristic time. Physically, for example, $\lambda(c) \sim 1/\dot{\gamma}_c(c)$, where $\dot{\gamma}_c(c)$ is the critical shear rate at which the plateau viscosity transitions to shear shinning at high shear rates. Eqn. 3 has been simplified from the Cross model used by eliminating the high shear rate viscosity from the functional form. This simplification is valid when the plateau viscosity $\eta_1(c)$ is much greater than the viscosity in the high shear rate limit. This limit holds our

measurements; in addition, this high shear rate regime is not accessible with our instruments. A consensus value of m = 0.6, as generated from preliminary fitting, was used in all cases. The value of $\sigma_0(c)$, the concentration dependent apparent yield stress, is not resolvable for the conditions of c ~75-80 mg/mL without urea, because the shear rate at which the stress achieves a plateau shifts to rates that are lower than the measurement range.

At concentrations below the entanglement concentration, the regime of shear thinning captured by the Cross model term is absent. In this case the model simplifies to the Bingham equation:

$$\eta(c,\dot{\gamma}) = \frac{\sigma_0(c)}{\dot{\gamma}} + \eta_1(c) \qquad \text{Eqn. 4}$$

The results of the fitting of Eqn. 3 and Eqn. 4 are shown in Figure 2.9 as solid lines; they describe the data well. The full set of fit parameters $\sigma_0(c)$, $\eta_1(c)$ and $\lambda(c)$ are reported in Table 2.1.

Table 2.1 Model Fit Parameters

No Urea

c / mg/mL	$\eta_1(c)$	$\lambda_c(c)$ / s	$\sigma_0(c)$ / Pa
3	3.90E-03	–	–
4	6.25E-03	–	–
5	8.77E-03	–	–
6.25	1.29E-02	–	–
7.5	1.89E-02	1.71E-04	6.51E-03
8.5	2.91E-02	3.27E-04	1.22E-02
10	4.32E-02	2.73E-04	9.37E-03
12.5	1.05E-01	8.29E-04	4.75E-02
18	2.73E-01	1.58E-03	8.17E-02
25	7.88E-01	3.68E-03	9.25E-02
28.75	1.80E+00	5.42E-03	3.34E-01
33	3.76E+00	1.28E-02	3.16E-01

40	8.97E+00	2.82E-02	1.06E+00
50	4.24E+01	1.68E-01	1.02E+00
55	6.80E+01	3.09E-01	9.86E-01
60	9.22E+01	4.27E-01	2.28E+00
65	4.33E+02	4.19E+00	2.89E+00
70	1.31E+03	1.73E+01	–
75	1.59E+04	6.24E+02	–
80	1.77E+04	5.58E+02	–

+ 4.0 M Urea

c / mg/mL	$\eta_1(c)$	$\lambda_c(c)$ / s	$\sigma_0(c)$ / Pa
3	5.19E-03	–	–
4	1.17E-02	–	–
5	1.02E-02	–	–
6.25	1.59E-02	–	–
7.5	1.91E-02	5.33E-05	–
8.5	2.99E-02	2.76E-04	–
10	5.35E-02	7.81E-04	–
12.5	9.37E-02	8.87E-04	–
18	2.97E-01	1.93E-03	3.70E-02
25	8.99E-01	2.77E-03	7.56E-02
28.75	1.47E+00	4.53E-03	8.95E-02
33	2.86E+00	7.63E-03	1.39E-01
40	5.36E+00	1.41E-02	2.27E-01
50	1.32E+01	3.30E-02	8.80E-01
55	2.53E+01	8.58E-02	2.55E+00
60	2.95E+01	7.61E-02	1.46E+00
65	4.19E+01	1.29E-01	1.04E+00
70	6.90E+01	2.13E-01	9.39E-01
75	5.74E+02	6.14E+00	–
80	7.43E+02	6.50E+00	–

The data in Figure 2.8 re-plotted as steady shear stress are shown in Figure 2.13 for concentrations where the low shear rate plateau in shear stress is apparent, c = 7.50 – 65 mg/mL without urea (Figure 2.13a) and c = 18.0 – 70 mg/mL with 4.0 M urea (Figure 2.13b). Select concentrations are compared with and without 4.0 M added urea in Figure 2.14. The low shear

stress plateau observed in Figure 2.14 could be indicative of yield stress behavior, of shear banding, or, potentially, of a combination of both phenomena. Our identification of the chitosan solutions as yield stress materials is appropriate because of the corroboration provided by the creep rheology measurements, which directly confirm the transition from elastic to viscous behavior, as characteristic of yielding either with or without shear banding.[48] The yield stress parameter $\sigma_0(c)$ extracted by the fits of Eqn. 3 is shown as a horizontal line in Figure 2.14; it is in good agreement with the observed plateau stress at low shear rates. As further validation of our model, the extracted yield stress from steady-shear viscosity modeling at c = 65 mg/mL of σ_0 = 3 Pa (from Eqn. 3) is in reasonably good agreement with the approximate yield stress range of 5-6 Pa determined from the creep tests (Figure 2.12).

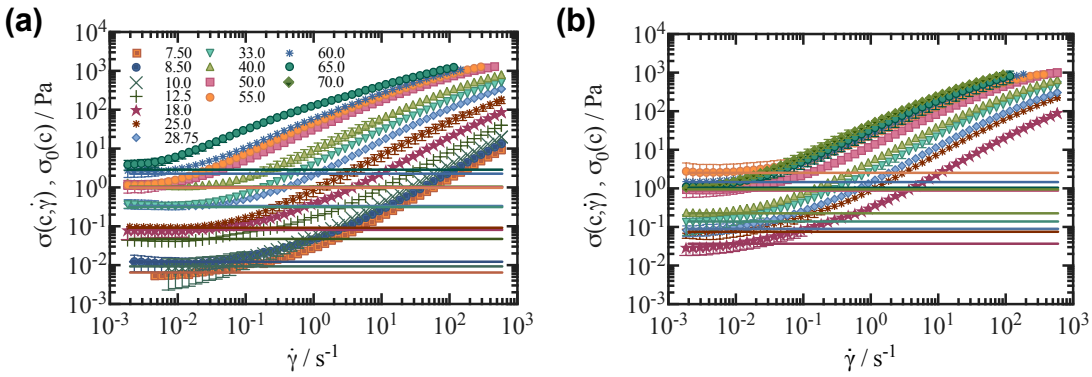

Figure 2.13 Steady shear stresswith and without added urea.
The steady shear stress of chitosan solutions in 0.3 M acetic acid and 0.15 M sodium acetate without (a) and with added 4.0 M urea. Data were collected as detailed in the Methods section of the paper. Selected concentrations are shown in Figure 2.14 in the main text of the paper.

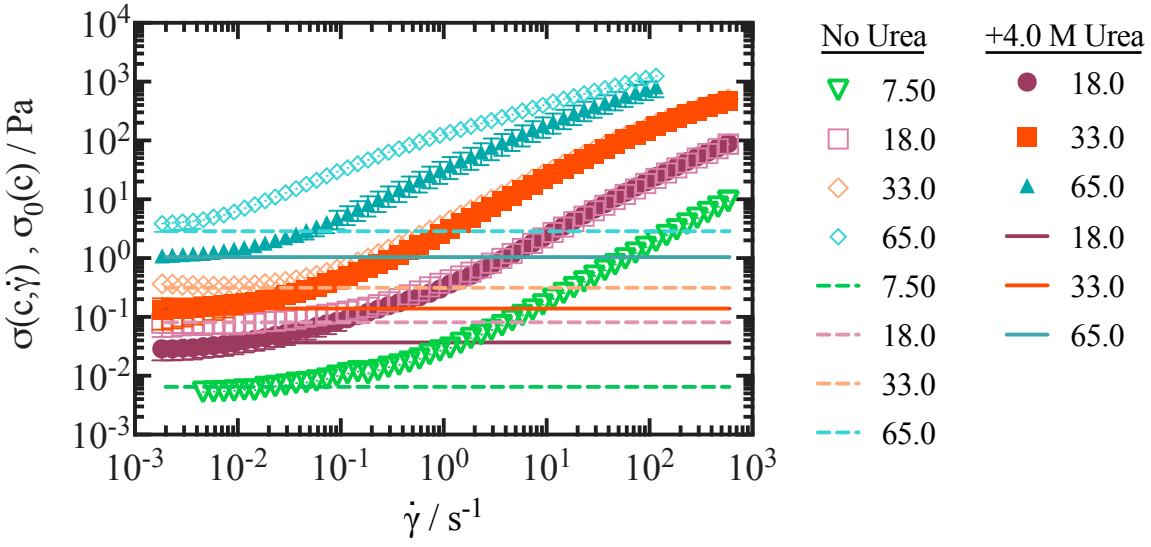

Figure 2.14 The shear stress $\sigma(c,\dot{\gamma})$ for chitosan solutions in the entangled regime without and with 4.0 M added urea.
Lines of $\sigma_0(c)$ were determined independently from viscosity modeling parameters (Eqn. 3). The full dataset is available in Figure 2.13.

2.5.3 Parameter Scaling

Figure 2.15 reports the scaling of the apparent yield stress with concentration for concentrations where the low shear rate plateau in the shear stress is apparent (see Figure 2.14). The data sets were fit to a power function $\sigma_0(c) \sim c^m$ with m = 2.8±0.2 without urea and m = 3.1±0.4 with 4.0 M added urea; the scaling exponents determined from the data are, to within experimental error, insensitive to urea addition. The magnitude of the apparent yield stress parameter is reduced by ~ 30% on average with the addition of 4.0 M urea, as determined over the full concentration range.

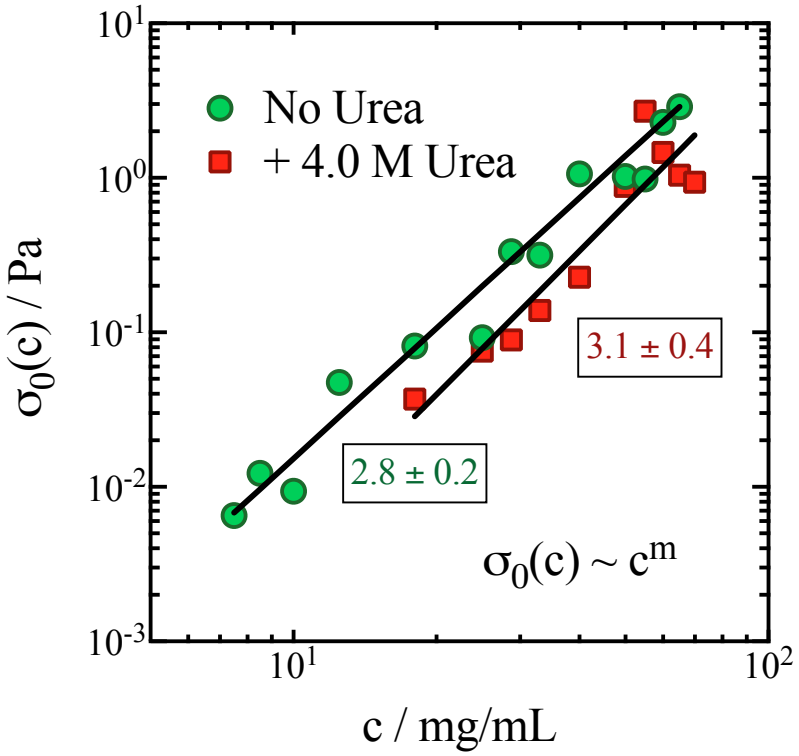

Figure 2.15 The yield stress parameter ($\sigma_0(c)$) from Eqn. 3 from steady-shear viscosity flow curve data (Figure 2.9).
Black lines represent power law fits; values in boxes represent exponent m.

We can also study the concentration dependent scaling of the extracted plateau viscosity. The reference concentrations reported in a previous section divide the physical behavior of the chitosan solutions into three regimes: the unentangled regime ($c < c_e$), the entangled regime ($c_e < c < c_g$), and the gelation regime ($c_g < c$). Figure 2.16 plots the specific intermediate-shear plateau viscosity $\eta_{sp,1}(c)$, defined as $\eta_{sp,1}(c) = \eta_1(c)/\eta_s - 1$ where η_s is the solvent viscosity. The plot characterizes the concentration dependence of the plateau viscosity at intermediate shear rates. For the unentangled and entangled regimes, $\eta_{sp,1}(c)$ was fit to a power law function with the constraint of continuity between the two concentration regimes. The fits are shown on Figure 2.16. The effect of urea on the scaling exponents is minimal.

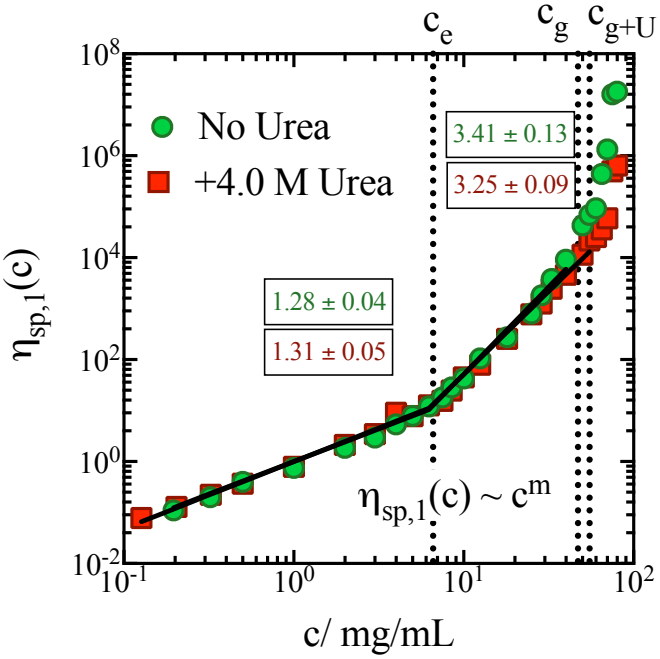

Figure 2.16 The specific intermediate-shear viscosity ($\eta_{sp,1}(c)$) from Eqn. 3-4 from viscosity flow curve data (Figure 2.9).
Black lines are power-law fits with the left-most points fixed for each concentration regime with and without added urea; values in boxes represent exponent m. All error bars represent standard error.

The regime of physical gelation is marked by a strong divergence from the power law scaling observed in the two low concentration regimes. The divergence is more rapid without urea than with 4.0 M added urea. At the highest concentration sampled, the addition of urea reduces the plateau viscosity by more than an order of magnitude relative to the no urea case. Further, the more rapid increase of $\eta_{sp,1}(c)$ for the without urea case is consistent with its lower gelation concentration. That is, with urea, the divergence of the viscosity is delayed, consistent with the difference in gelation concentration (c_g = 55 mg/m for with urea versus c_g = 47 mg/ml for without urea).

2.5.4 Dynamic Light Scattering (DLS)

To probe the quiescent solution behavior at high concentrations, Figure 2.17 compares the q-dependent dynamic structure factor, f(q,t), of c = 40 mg/ml and c = 65 mg/ml chitosan solutions as per the Methods. The DLS measurements at both concentrations and for all scattering vectors exhibit a two-step relaxation in f(q,τ). We find that the short-time decay is exponential and the long-time decay event is stretched exponential.

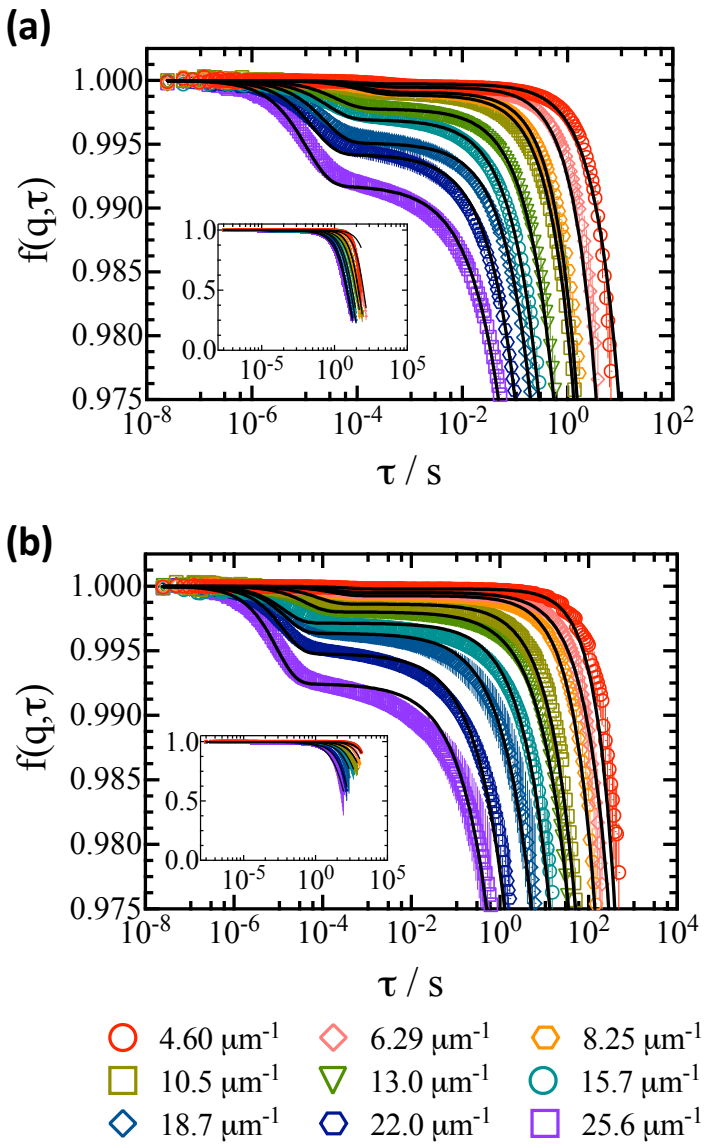

Figure 2.17 Measured $f(q,\tau)$ data (open circles) for c = 40 mg/mL from Eqn. 1 (a) and for c = 65 mg/mL from Eqn. 2 (b).
Fits are to Eqn. 5. The insets show the full data set that is expanded in the main figure to resolve the short lag time region of the first decay event.

Therefore, Eqn. 5 below was adopted to model the observed decay events, where β(q) is the argument of the stretched exponential of the slow relaxation, A(q) and (1-A(q)) are the fast

and slow decay amplitudes, respectively, and $\tau_\alpha(q)$ and $\tau_\beta(q)$ are fast and slow decay constants, respectively:

$$f(q,\tau) = A(q)e^{-(\tau/\tau_\alpha(q))} + (1 - A(q))\, e^{-\left(\tau/\tau_\beta(q)\right)^{\beta(q)}} \qquad \text{Eqn. 5}$$

The measurements were fit by minimizing a weighted residual. The weighting function was the inverse of the square of the standard error of $f(q,\tau)$. The average relaxation time of the stretched process $\langle\tau_\beta\rangle$ was calculated using Eqn. 6 below.

$$\langle\tau_\beta\rangle = \frac{\tau_\beta}{\beta}\Gamma\left(\frac{1}{\beta}\right) \qquad \text{Eqn. 6}$$

Decay constants $\tau_\alpha(q)$ and $\tau_\beta(q)$ are plotted in Figure 2.18. The amplitude of the fast decay event was the same for c = 40 mg/mL and c = 65 mg/mL and scaled as $A \sim q^{2.02\pm0.05}$ (c.f. Figure 2.19). That is, the fast mode makes a progressively larger contribution to the dynamic structure factor as q is increased. In addition, the value of $\beta(q)$ progressively decreased with q from a value of 1 to 0.65; $\beta(q)$ is plotted in Figure 2.20.

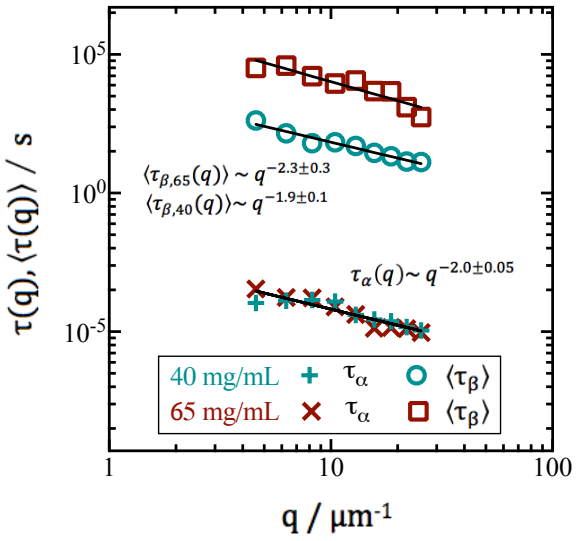

Figure 2.18 Fit parameters $\tau_\alpha(q)$ and $\tau_\beta(q)$ from Eqn. 5 for c = 40 mg/mL and c = 65 mg/mL.
Solid lines report power law fits of the data.

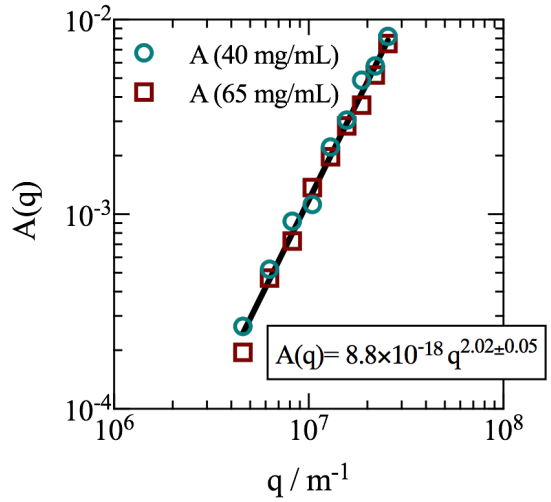

Figure 2.19 Mode Amplitudes from DLS data fitting.
The measured f(q,τ) shown in Figure 2.17 were fit using Eqn. 5 to obtain the mode amplitude A(q). The value of A(q) for c = 40 mg/mL and c = 65 mg/mL is shown in Figure 2.19. A(q) is concentration independent and scales as $A(q) = 8.8 \times 10^{-18}\ q^{2.02\pm0.05}$.

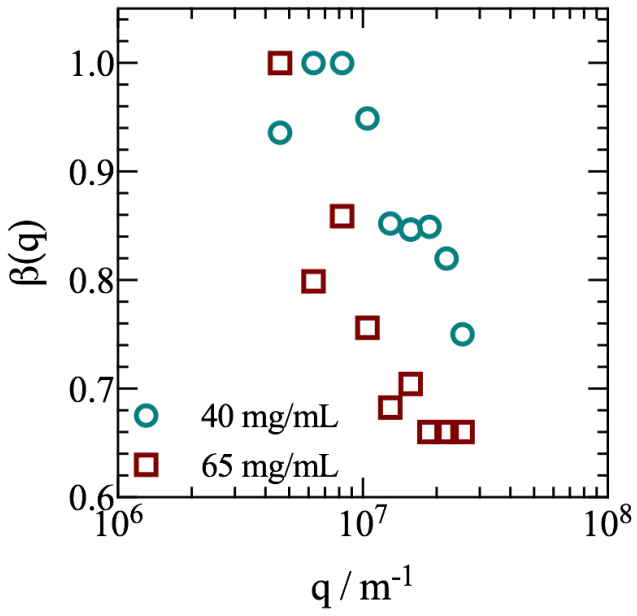

Figure 2.20 Stretched exponential argument from DLS data fitting.
The measured f(q,τ) shown in Figure 2.17 were fit using Eqn. 5. The argument of the stretched exponential β(q) was constrained to 0.65-1.

The scaling of $\tau_\alpha(q)$ and $\tau_\beta(q)$ with q was determined by fitting the unweighted data to a power function to obtain $\tau_\alpha(q) \sim q^{-2.0\pm0.05}$ (for both concentrations), $\tau_{\beta,40}(q) \sim q^{-1.9\pm0.1}$ for c = 40 mg/ml and $\tau_{\beta,65}(q) \sim q^{-2.3\pm0.3}$ for c = 65 mg/ml; these fits are also shown in Figure 2.17. Because of the stretched exponential relaxation, the slow mode for each concentration is not diffusive, even though the q-scaling for c = 40 mg/ml is quadratic and that for c = 65 mg/ml is nearly so.

2.6 Discussion

This study has reported a region of low-rate shear thinning consistent with an apparent yield stress in aqueous solutions of chitosan for a wide concentration range of 3 – 80 mg/mL. Creep measurements at c = 65 mg/mL confirm a transition from yielding to flow at values of applied stress that agree with the modeling of the steady-shear viscosity measurements. Urea, a

disruptor of hydrophobic interactions and hydrogen bonding, increases the gel point of chitosan solutions and reduces the apparent yield stress. However, it does not strongly affect the concentration dependent plateau viscosity observed at intermediate shear rates below the gel point or the scaling of the apparent yield stress parameter. Further, the microdynamics of these solutions, as measured by dynamic light scattering, exhibit a slow mode with stretched exponential relaxation consistent with slow dynamics. This DLS characterization complements recent images of dried chitosan solutions obtained using wet-STEM with concentrated solution microdynamics.[10]

In this discussion we address (i) the scaling of chitosan solution viscosity in the intermediate-shear rate regime in the context of theories developed for polymer solutions that are entangled and associated; (ii) the scaling of the yield stress on concentration in light of existing microstructural models of soft materials, and (iii) the observed microdynamics of the chitosan solutions.

Scaling of plateau viscosity in the intermediate shear-rate regime. Below the gel point the scaling exponent, m, of $\eta_{sp,1}(c) \sim c^m$ as reported in Figure 2.16 is consistent with previously reported scaling exponents for chitosan solutions.[82,85,86] In the dilute concentration regime, the viscosity scaling exponent (m = 1.28) agrees with reported values of other polysaccharide systems (m = 1.2 – 1.3).[89] The scaling exponent in the semi-dilute entangled concentration regime (m = 3.4) is only slightly lower than the predicted scaling for polyelectrolytes in excess salt (m = 3.8)[110] and for entangled, associating polymers in a good solvent (m = 3.9).[111] It is more significantly lower than the expected scaling for semi-dilute, entangled polymer solutions

in a good solvent (m = 4.25).[112] Thus, the measured exponent is more consistent with a contribution of associative and polyelectrolyte effects than not. Note that above the gel point, the strong concentration dependence of the plateau viscosity is consistent with exponential scaling models of associating polymers with large aggregates, and in fact this study's measurements in this regime could equally well be modeled as an exponential rather than a power law function.[113]

The addition of urea increased the gel point by 15% and reduced the plateau viscosity above the gel point, suggesting that at high concentrations hydrophobic associations and hydrogen bonding effects – which are moderated by urea addition – do contribute to the solution viscosity. However, at concentrations lower than the gelation regime, urea has a limited effect on the plateau viscosity. The insensitivity of chitosan rheology to urea addition is consistent with previous reports[16,91–93] and highlights the need for further characterization of the nature of interactions in chitosan associations.

The yield stress and its implications for chitosan microstructure. The observed scaling of the yield stress with concentration, $\sigma_0(c) \sim c^{2.8\pm0.2}$ and $\sigma_0(c) \sim c^{2.9\pm0.3}$ without and with urea, respectively are comparable to the reported scaling of $\sigma_0(c) \sim c^{3.0}$ in percolated dispersions of carbopol 940 mirogels[114] and $\sigma_0(c) \sim \phi^{3.3}$ in silica-silicone physical gels with a fractal structure.[115] Other fractal cluster rheological models[116,117] can equally well explain the yield stress scaling as a consequence of the existence of fractal clusters in the chitosan solutions.

In fractal cluster models of microstructure, the material's microstructure is a disordered fluid of clusters; the clusters themselves display fractal scaling of density within.[118] For fractal

clusters of this kind, the scaling of $\sigma_0(c)$ has been reported to depend on the fractal dimension (d_f) as $\sigma_0(c) \sim c^{4/(3-d_f)}$.[115] If the scaling of $\sigma_0(c)$ reported in this communication is attributed to a shear-sensitive concentration-dependent fractal microstructure, the fractal dimension of the quiescent solution can be extracted as $d_f = 1.6 \pm 0.2$ without and $d_f = 1.7 \pm 0.4$ with urea, consistent with diffusion-limited cluster aggregation. The effect of urea on the apparent yield stress is modest; it lowers the apparent yield stress by ~ 30%, without modifying the underlying scaling exponent. Thus, we conclude that the measured yield stress of the chitosan solutions is consistent with fractal cluster microstructure.

Chitosan solution microdynamics. DLS probes the thermodynamic (quiescent) limit, which low-shear rheology may or may not access. Nevertheless, insight from DLS is useful to interpreting the rheology as such quiescent microstructure likely persists in the very low-shear conditions of the rheological testing. The microdynamics of the chitosan solutions of c = 40 mg/mL and c = 65 mg/mL are well modeled by two relaxation modes. Considering first the fast mode, which shows exponential relaxation, the diffusion coefficient of the fast mode, D_α, is calculated from $\tau_\alpha(q) = D_\alpha q^2$ as $D_\alpha = 13\ \mu m^2/s$. Using the Stokes-Einstein equation, D_α is consistent with a characteristic size of ~ 17 nm for both concentrations probed. Often, this mode is interpreted as the correlation length (ξ) or average mesh size of a polymer network.[119] However, the origin of the fast mode in chitosan solutions is not consistent with representation as a correlation length due to its concentration independence; this independence also has been reported in hydrophobically modified chitosan micelle networks[120] as well as in solutions of unmodified chitosan.[38,121] The fast relaxation may alternatively represent the relaxation time of a single chitosan coil, the hydrodynamic size of which is ~30 nm (c.f. Figure 2.1), comparable to

the characteristic scale that generates the fast relaxation process. However, definitive assignment of the origin of the fast relaxation time is not possible without eliminating other modes like strand relaxation; this subject merits further investigation.

The time scales of the slow modes of the two concentrations differ significantly. Interestingly, the fact that the c = 40 mg/mL specimen is ergodic and the c = 65 mg/mL specimen is non-ergodic is consistent with the calculated gel point (c_g = 47 mg/mL) being located between these two limits. Further, the slow mode in both concentrations studied shows extremely slow, arrested dynamics reflective of colloidal liquids close to the gel point,[122] colloidal gels[122] or glassy liquids.[123] The slow dynamics of the chitosan solutions – with relaxation times greater than or equal to thousands of seconds on submicron scales – further support the yield stress phenomenology reported by steady-shear and creep measurements. Although DLS provides indirect evidence for these structures, additional understanding could be gained by direct visualization with advanced microscopy techniques like wet-STEM.

2.7 Conclusion

In conclusion**,** there is evidence of a yield stress in high molecular weight chitosan solutions based on the shear thinning of the apparent viscosity at low shear rates. Solution microdynamics confirm the presence of a large, non-diffusive microstructure consistent with the observed yield stress behavior. The scaling of the concentration-dependent yield stress is consistent with the existence of a fractal cluster microstructure, as is commonly observed in aggregated systems. The shear rheology of chitosan depends on these microstructural properties at low shear rates; the molecular character of the polymers becomes more apparent at higher

shear rates, beyond the yield stress regime. In this region, the solutions are yielded, and the viscous scaling is consistent with semi-dilute entangled rheology, modified by associative and/or polyelectrolytic effects. Hydrophobic effects and hydrogen bonding have limited effect on these physics, as demonstrated, for example, by the fact that added urea reduces the yield stress by only ~ 30%.

Chapter 3

Flow Characterization and Shear Banding in Chitosan Solutions

3.1 Abstract

Self-associating chitosan solutions exhibit a plateau in the flow curve at low shear rates. This phenomenon has been associated with yield stress behavior; however, in other systems comparable behavior has been shown to be the consequence of shear banding. The existence of shear banding has not been addressed in self-associating chitosan solutions. In order to characterize the flow in such chitosan solutions, a rheo-optical instrument was used to measure the velocity profile in the gap between parallel plates. Silicone oil was applied around the gap to prevent rapid sample evaporation. The addition of silicone oil introduces new experimental challenges as a result of image distortion as well as new secondary flows, as evidenced by the observation of non-linear velocity profiles in standard solutions of polyethylene oxide (PEO) and silicone oils at low shear rates and stresses. To validate our modified experimental conditions, we carefully evaluated lower stress and shear rate limits, excluding regions of flow adversely affected by the application of the silicone oil. We find that in the experimentally valid shear rate range of $\dot{\gamma} = 0.01 - 0.056\ s^{-1}$ chitosan solutions of c = 40 mg/mL and c = 65 mg/mL do not exhibit shear banding. The shear rate range of characterization, although significantly lower than most literature measurements, does not completely rule out the possibility of shear banding in self-associating chitosan solutions. To extend the shear rate range to lower shear rates, a secondary characterization technique would be necessary. However, the studied shear rate range

does overlap with the region of plateau behavior; this provides the suggestion that shear banding is not occurring in these solutions.

3.2 Background

In the previous chapter, we showed that the rheology of high molecular weight chitosan solutions is dominated by solution microstructure at low shear rates and molecular properties at high shear rates. The measured flow curve features a region of shear thinning in the low shear rate region consistent with an apparent yield stress.[45] In shear banded flows, bands of distinct shear rates and viscosities coexist within the sheared sample. Steady-state shear-banded flows are a common feature of yield stress fluids[48] and are often associated with shear-induced re-structuring of the fluid.[43] Distinct bands as well as highly curved velocity profiles have been observed in solutions of concentrated xanthan gum, a highly charged polysaccharide.[49] However, shear banding in polysaccharide solutions, including chitosan, has largely been unexamined. The purpose of the measurements reported in this chapter is to test for the possible existence of steady-state shear banding in chitosan solutions within the low stress plateau region of the flow curve.

The rheological constitutive equation of a material relates the shear stress with the deformation history.[36] In shear banding fluids, the underlying constitutive relationship can yield a non-monotonic flow curve in which the measured shear rate is predicted to decrease over a range of shear stresses. Because a decrease in stress with shear rate is unstable, the flow splits into domains of high and low shear rates. Overall, a stress plateau is observed.[124] Also, the transmission of force in a complex fluid may be localized resulting in stress heterogeneity, a

disparity between the local and average stress.[47] In simple, non-thixotropic yield stress fluids – like chitosan solutions, and also, for instance, microgels, dense emulsions, and foams – the flow curve is not necessarily non-monotonic, but stress heterogeneity can lead to shear banding if the local shear stress falls below the yield stress.[48,125]

Velocity fields during shear have been characterized using nuclear magnetic resonance (NMR),[126] particle tracking velocimetry,[44,127,128] dynamic light scattering (DLS) and ultrasonic speckle velocimetry (USV).[129] In this chapter, we characterize the steady-state flow of high molecular weight chitosan solutions. These solutions are the same as those studied in the previous chapter. Here, these solutions are doped with fluorescent tracers whose motion is tracked by video microscopy. Particle tracking velocimetry is applied to videos that capture the tracer motion using a rheo-microscope, as reported in Wei et al.[44]

The addition of a layer of silicone oil was necessary to prevent laser induced sample evaporation. The cost of evaporation mitigation was reduced image quality and the introduction of secondary flows, presumably generated as a result of the gravitationally driven downward flow of the externally applied silicone oil. This flow may become significant at low applied shear rates where the experimental window is long. As such, polymer standards were used to validate both the low shear rate and low stress limit of the modified experimental conditions.

The analysis of chitosan flow stability presented here contributes to the understanding of the rheology of chitosan solutions as well as, more broadly, the identification of the potential for shear banding in aqueous solutions of polysaccharides.

3.3 Experimental Methods

3.3.1 Materials

High molecular weight chitosan from Heppe Medical Chitosan GmbH (Halle (Saale), Germany) was used as received. Solutions of c = 40 mg/mL and c = 65 mg/mL were prepared using HPLC-grade water, 0.3 M acetic acid, and 0.15 M sodium acetate. The fraction of de-acetylation is 72%, from triplicate CHN elemental analysis by Elemental Analysis, Inc. (Lexington, KY) as in dos Santos et al.[98] The weight averaged molecular weight (M_W) was 8.2 ± 0.4 × 10^5 g/mol from static light scattering (SLS) using a Zimm plot analysis (with compact goniometer system CGS-3, ALV GmbH, Langen, Germany) of four dilute concentrations.[45]

Four silicone oils of η_0 = 1, 5, 30 and 100 kPa.s were used from AMETEK Brookfield as standards. To approximate the viscous behavior of chitosan solutions, two additional standards of 5 and 8 wt.% polyethylene oxide (PEO) with M_w = 1,000,000 Da from Polysciences Inc. were considered to determine the minimum shear rate. In all solutions, Fluoresbrite® Plain YG microspheres of d = 3.06 μm (Polysciences Inc.) were added for particle tracking at a volume percent of 0.014. Samples were rolled at 0.9 rpm for ~ 1 week before analysis. Silicone oil of η_0 = 1 kPa.s (AMETEK Brookfield) was externally applied to the gap in all tests using a cotton tipped swab in order to control rapid sample evaporation. This was a necessary step for chitosan and PEO solutions and was done for the silicone oil standards for consistency.

3.3.2 Shear banding measurements

Shear banding measurements were performed using an MCR 702 TwinDrive rheometer (Anton Paar) operating in constant strain mode with a 50 mm stainless steel parallel plate bottom

geometry and a 50 mm brushed stainless steel parallel plate top geometry at a gap height of 0.25 mm. All measurements were performed at room temperature. A schematic representation of the experimental setup is shown in Figure 3.1a. The viscosity (η) and shear stress (σ) were measured at each shear rate sampled. Tracer particles were imaged in the velocity gradient plane at the outer edge of the parallel plate flow by means of fluorescence microscopy. Videos were recorded with an Lw165R 1.4 megapixel camera (Lumenera, Ottawa, Ontario) at 15 fps, under an EL6000 external light source (Leica microsystems CMS Gmbh, Wetzlar, Germany) passed through a band pass filter of 450-490 nm (Anton Paar). A still image of a c = 65 mg/mL chitosan solution with added tracers is shown in Figure 3.1b. The optical distortion from silicone oil application is apparent in the crosshatched or dashed shape of the spherical tracers (c.f. Figure 3.1b).

All samples were sheared at σ = 14. 1 Pa for two minutes followed by a rest period of five minutes. Measurements were performed in the shear rate range of $\dot{\gamma} = 10^{-4} – 10^{-1}$ s^{-1} for silicone oil standards and $\dot{\gamma} = 10^{-3} – 10^{-1}$ s^{-1} for PEO standards and chitosan solutions. For all samples, data were collected at a sampling density of four shear rates per decade. For chitosan solutions, the sample was sheared at the set shear rate for a period of 10 minutes before video collection to ensure the steady-state flow was characterized; however, no transient behavior was observed. For all samples, videos of sufficient length to ensure significant displacement of tracers for velocity extraction were collected; the length of video varied from 17 minutes at $\dot{\gamma}= 10^{-3}$ s^{-1} to a minimum time of 2 minutes for $\dot{\gamma} > 10^{-2}$ s^{-1}.

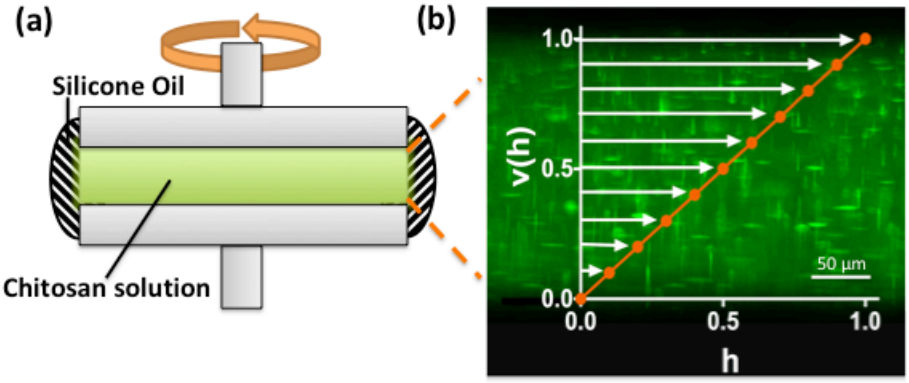

Figure 3.1 Experimental Set-up.
(a) Schematic cross-section of chitosan solution doped with fluorescent tracers inside two parallel plate geometries coated in silicone oil (b) Chitosan solution of c = 65 mg/mL with 3 µm fluorescent tracer imaged through silicone oil overlaid by the normalized velocity v(h) as a function of normalized gap height (h) for an ideal linear flow with DOB = 0.

3.3.3 Rheological Measurements

The steady shear viscosity of c = 40 mg/mL and c = 65 mg/mL chitosan solutions was collected using an AR-G2 rheometer (TA Instruments) as detailed in Gasbarro and Solomon.[45]

3.3.4 Particle image velocimetry (PIV)

Velocity profiles in the gradient direction were calculated using an image analysis tool for simple shear flows as in Wei et al.[44] Briefly, this method performs the following operations on video images. First, the images are converted to black and white using contrast-limited adaptive histogram equalization to improve contrast; second, images are divided into horizontal ribbons of two pixels in height; third, the average vertical intensity across each ribbon is converted to a normalized value; fourth, the normalized value is cross-correlated over a specified time interval. For three samples, the velocity at fourteen different time points was averaged. The normalized vertical gap position (h) is calculated as $h = (px - px_{min})/(px_{max} - px_{min})$ where px is the location of an arbitrary pixel in the gap plane, px_{min} is the location across the bottom plate,

and px_{max} is the location across the top plate. The normalized velocity v(h) is defined as v(h) = $u(h)/u(h)_{max}$ where u(h) is the un-normalized velocity extracted from cross-correlation. For a fully linear flow, v(h) is shown superimposed on a frame in Figure 3.1b.

To characterize the linearity of the velocity profile, the degree of banding – DOB – was selected to represent the deviation from linear, homogenous flow on an area basis as in Wei et al.[44] The DOB ranges from 0 to 1 to describe the extreme cases of plug and linear flows, as shown in Eqn. 1:

$$\mathrm{DOB} = 2\int_0^1 |v(h) - h| dh \qquad \text{Eqn. 1}$$

To find the experimental range where flow can be studied without image distortion or interference from secondary flows, standards were used to probe the distortion of the flow.

3.4 Results

3.4.1 Determination of the low shear stress limit with standards

Four silicone oil standards were evaluated to determine the effect of externally applied silicone oil on the minimum shear stress limit. The extracted v(h) is shown in Figure 3.2 for each sampled shear rate and standard. The dip in v(h) for the 5 kPas silicone oil standard for $\dot{\gamma} > 5.6 \times 10^{-3}\ s^{-1}$ – particularly noticeable at $\dot{\gamma} = 1.8 \times 10^{-2}\ s^{-1}$ (c.f. Figure 3.2) – is thought to be the result of undoped externally applied silicone oil mixing with the doped standard at the imaged interface and forming a transient horizontal band; the dip in v(h) is the result of this band and not the fluid flow. Here doped refers to the addition of tracer particles.

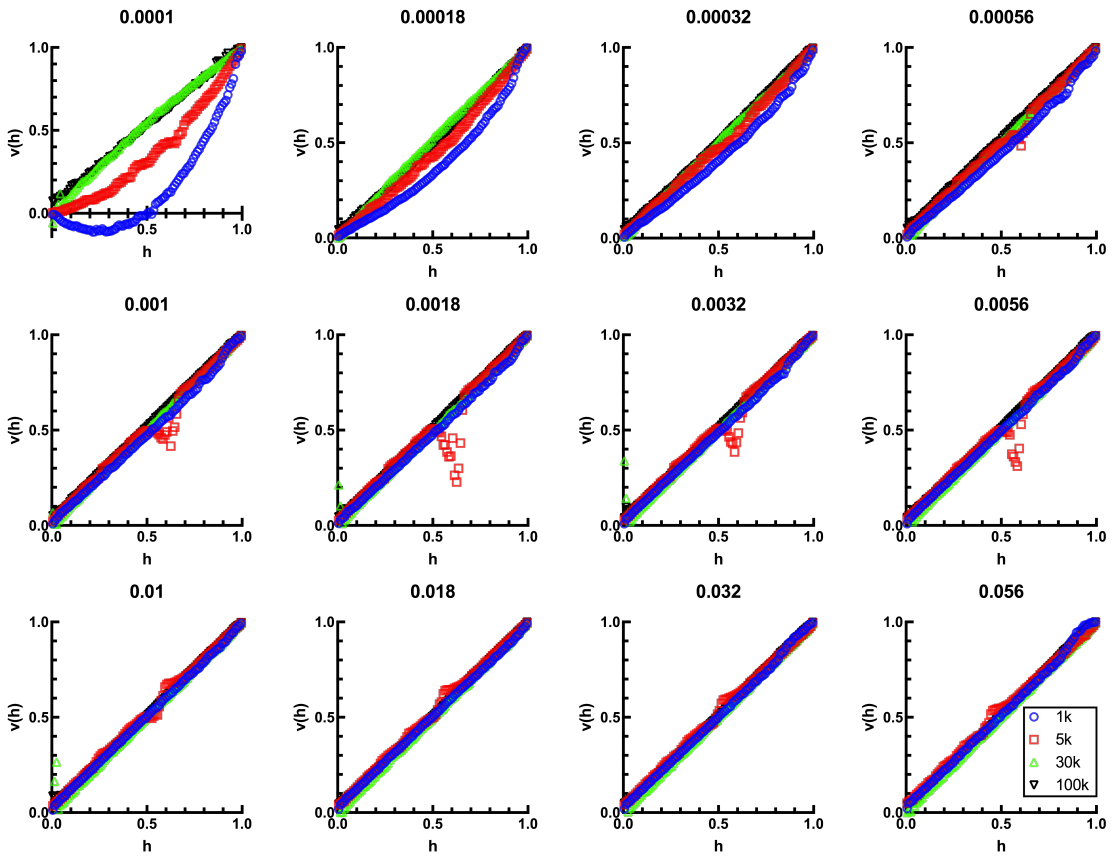

Figure 3.2 The normalized local velocity v(h) of four silicone oil standards of η = 1, 5, 30 and 100 kPas at twelve shear rates from $\dot{\gamma} = 10^{-4} – 10^{-1}$ s^{-1}.

There is a clear deviation from the linear velocity profile expected for these fluids over the shear rate range of $\dot{\gamma} = 1 \times 10^{-4} – 5.6 \times 10^{-4}$ s^{-1} for the 1 and 5 k Pas standards. The extracted v(h) for higher viscosity standards of 30 and 100 kPas appear linear, as is consistent with viscometric flow.

The DOB for each shear rate and viscosity standard is computed from the Figure 3.2 measurements using Eqn.1 and plotted as a function of measured shear stress (σ) in Figure 3.3. The plateau observed in Figure 3.3 in the high stress regime is greater than zero due to distortions in image quality (apparent in Figure 3.1b). The plateau instead approaches a value of

~0.05, which is taken as a baseline. In addition, because the DOB is constructed as a positive quantity, the DOB will deviate from zero as the result of noise in the velocity profile, even for random error.

Below $\tau = 0.1$ Pa, the DOB(σ) for standards of 1 and 5 kPas viscosity significantly deviates from ~0.05, and a slight DOB upturn in the 30 and 100 kPa data is also apparent. A minimum shear stress of $\tau = 0.1$ Pa was determined for use in all chitosan solution testing. This limit was below the minimum shear stress used for both concentrations of chitosan used. Thus, the minimum shear stress was not a limiting factor in our experimental setup.

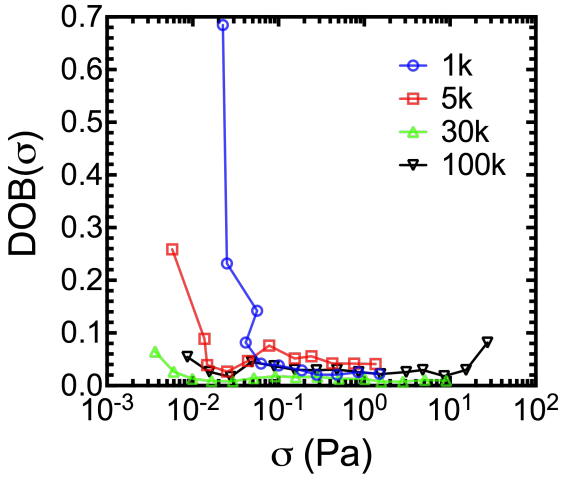

Figure 3.3 DOB(σ) was calculated using Eqn. 1 from v(h) shown in Figure 3.2 for four silicone oil standards of η = 1, 5, 30 and 100 kPa.s.

3.4.2 Determination of the low shear rate limit

Two silicone oil standards (η = 30 and 100 kPas) are significantly more viscous than the chitosan solutions considered here. These standards display an approximately linear v(h) over the full range of shear rates sampled. These shear rates are as low as $\dot{\gamma} = 10^{-4}$ s^{-1} (c.f. Figure 3.2).

However, from Figure 3.2, this is not the case for the standards of lower viscosity. To better probe the transition from linear to non-linear v(h) for solutions with a low viscosity that approximates that of chitosan solutions, two PEO solutions of 5 and 8 wt.% were considered. The extracted v(h) is shown in Figure 3.4.

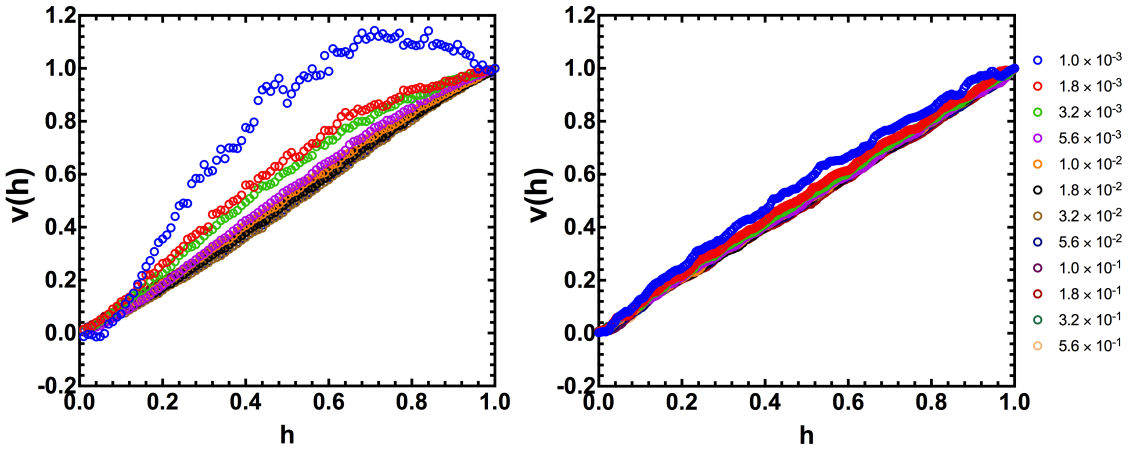

Figure 3.4 v(h) for standard solutions of 5 wt.% (a) and 8 wt.% (b) PEO at twelve shear rates

For both PEO standards, v(h) is a non-linear function at low shear rates (c.f. Figure 3.4). This is especially apparent in the 5.0 wt.% PEO sample at $\dot{\gamma} = 10^{-3}$ s^{-1} where portions of v(h) fall outside the expected range of v(h) = 0 – 1, shown in Figure 3.4a. The DOB was calculated from v(h) in Figure 3.4 using Eqn. 1 and plotted along with the DOB from $\eta = 1$ and 5 kPas silicone oil standards taken from Figure 3.3, as shown in Figure 3.5. As in Figure 3.3, the degree of banding converges to a baseline of $DOB(\dot{\gamma}) \sim 0.05$ instead of zero at high shear rates as a result of image distortion (c.f. Figure 3.1b) and experimental noise. If the observed deviation in DOB at low shear rates is induced by the downward flow of silicone oil under gravity, some variability in the observed convergence is expected, as the downward velocity is sensitive to the variable

thickness of the applied silicone oil layer. For all standard solutions, this convergence is complete by $\dot{\gamma} = 10^{-2}\ s^{-1}$.

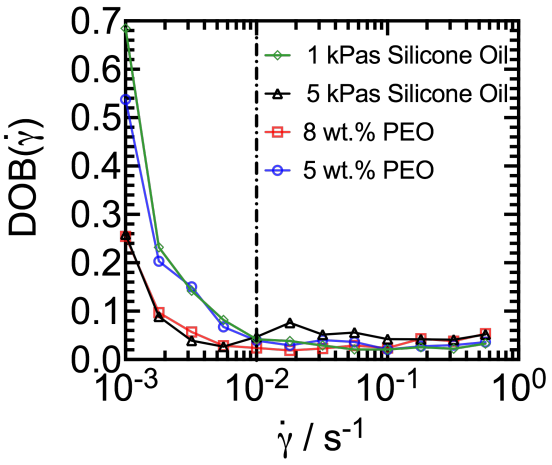

Figure 3.5 DOB($\dot{\gamma}$) of four standard solutions of silicone oil and PEO. The dashed line at $\dot{\gamma} = 10^{-2}\ s^{-1}$ shows the selected low shear rate limit.

3.4.3 Characterization of chitosan solutions

To summarize the results of the prior sections, we expect that we will obtain valid characterization of chitosan solutions using the device for applied shear stresses greater than $\tau =$ 0.1 Pa and applied shear rates greater than $\dot{\gamma} = 10^{-2}\ s^{-1}$. The measured velocity profiles for c = 40 mg/mL and c = 65 mg/mL are shown in Figure 3.6a and b respectively for four shear rates above the minimum shear rate and stress limits. For both concentrations, v(h) is linear across the gap, with only a slight curvature from distortion in the collected image (c.f. Figure 3.1b) and/or experimental noise.

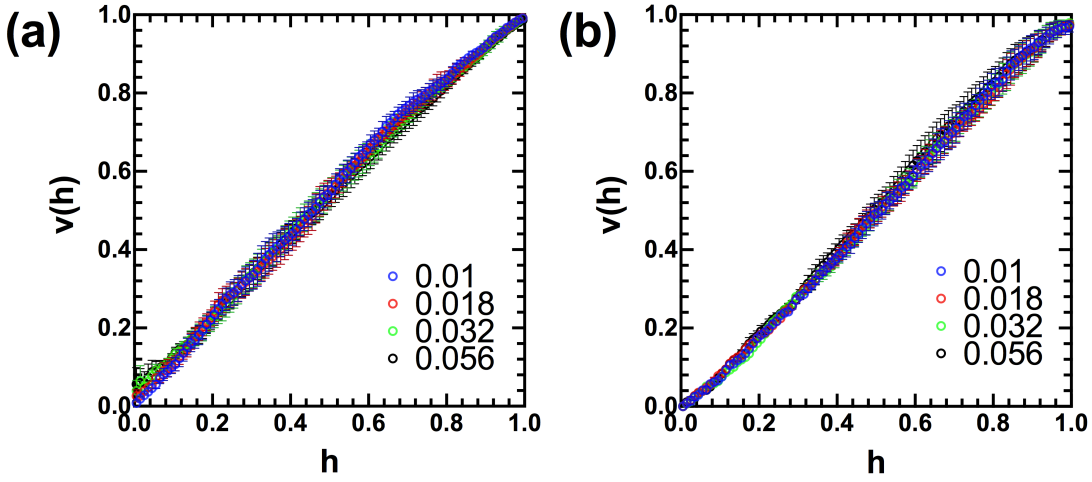

Figure 3.6 v(h) for chitosan solutions of (a) c = 40 mg/mL (b) and c = 65 mg/mL at four shear rates.

The DOB($\dot{\gamma}$) for both concentrations of chitosan solution from Eqn. 1 is shown in Figure 3.7. For both concentrations and shear rates, we report a constant DOB of ~0.05, consistent with the noise level observed in the baseline of standard samples (c.f. Figure 3.3 and Figure 3.5).

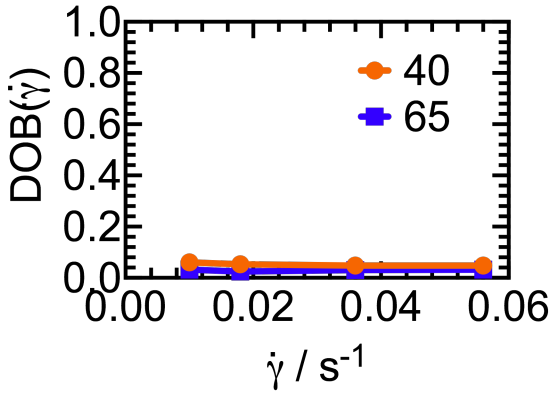

Figure 3.7 The DOB($\dot{\gamma}$) for two solutions of c = 40 mg/mL chitosan (orange) and c = 65 mg/mL chitosan (blue) as calculated from Eqn. 1 using v(h) shown in Figure 3.5.

.

3.5 Discussion

This study has demonstrated that the penalty for eliminating rapid sample evaporation in aqueous solutions by means of the application of an externally applied, low viscosity silicone oil is twofold: (1) elevation in the baseline DOB($\dot{\gamma}$) and (2) limiting the working shear rate range to $\dot{\gamma} \geq 0.1\ s^{-1}$. The elevation in the DOB($\dot{\gamma}$) baseline is a consequence of the distortion of individual frames from imaging through a silicone oil layer apparent in Figure 3.1b in addition to random noise. Further, through careful analysis of PEO and silicone oil standards, we see deviation of the flow from linear behavior at low shear rates. This non-linearity in v(h) leads to DOB values that are as large as fourteen times the baseline (c.f. Figure 3.3 and Figure 3.5).

The externally applied silicone oil flows under gravity. The evidence for this statement is that occasional drops of silicone oil were observed to have fallen directly under the coated geometry. From the Navier-Stokes equations, for a fluid film flowing under gravity on a stationary surface, the maximum velocity v_{oil} scales as $v_{oil} \sim d^2\eta^{-1}$ where d is the thickenss of the film and η is the film viscosity. The thickness of the film was not carefully controlled, and this may result in variability in the velocity of secondary flows. The variability in the minimum $\dot{\gamma}$ to reach the baseline DOB($\dot{\gamma}$) value, sometimes below the selected minimum of $\dot{\gamma} = 0.01\ s^{-1}$, (c.f. Figure 3.5) may therefore be due to differences in the specific details of how the silicone oil film was applied. Secondary flows may be reduced with a higher viscosity silicone oil coating for flow visualization, although this solution could also introduce new additional experimental issues.

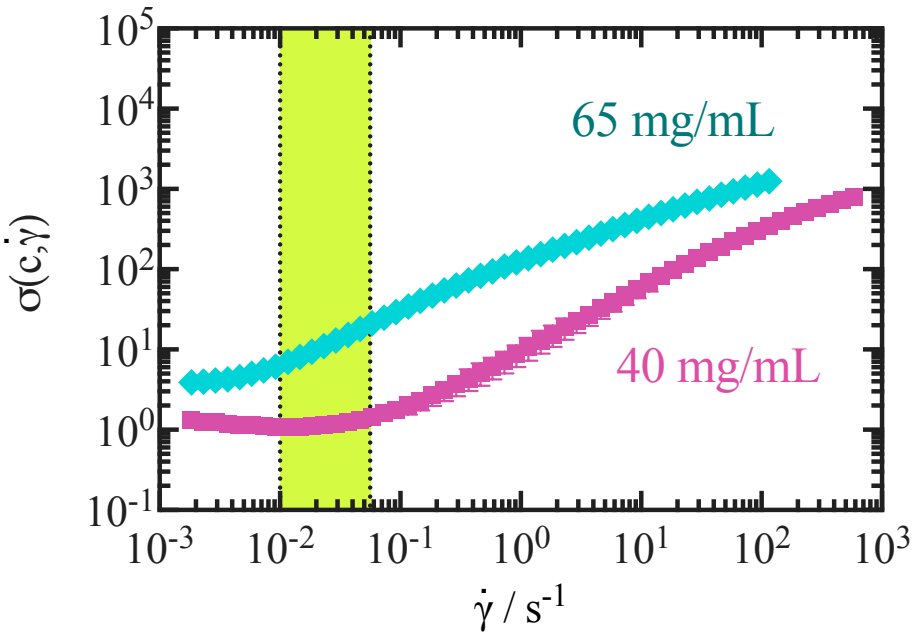

Figure 3.8 Flow curves for c = 40 mg/mL and c = 65 mg/mL from [45] with the region imaged in this study highlighted in yellow-green.

While the valid shear rate range for flow imaging is limited, the allowable range does extend into the region of interest for understanding the behavior of self-associating chitosan solutions. The stress plateau for the c = 40 mg/mL chitosan solution, in which we are interested in identifying whether or not shear banding is occurring, is partially accessible in our flow visualization as shown in Figure 3.8. (The plateau region for the c = 65 mg/mL chitosan solution is not – c.f. Figure 3.8). In addition, the limits identified are well below the ranges that in which shear banded flows have been typically characterized.[44]

The lack of observation of shear banded flow in the accessible region of the 40 mg/mL chitosan solution stress plateau (the region indicated by the vertical stripe on the figure) indicates that shear banding alone is not an explanation for the stress plateau, and this phenomenon may instead be associated with yield stress behavior. We cannot definitively rule out that the full

plateau region is devoid of shear bands by means of this study. Nevertheless, the finding does provide a degree of confidence that the yield stress of self-associating chitosan solutions is not accompanied by banded flow.

3.6 Conclusion

The low shear rate plateau in the flow curve of chitosan solutions has been associated with yield stress behavior;[45] however, in other systems comparable behavior has been shown to be the consequence of shear banding. To evaluate shear banding in the stress plateau, a rheo-optical setup was utilized to characterize the flow velocity in the geometry gap and calculate the degree of banding (DOB) for two chitosan solutions of c = 40 mg/mL and c = 65 mg/mL. An external layer of silicone oil was added to the gap to prevent rapid sample evaporation but introduced new challenges in that (1) subsequent image distortion caused an elevation in baseline DOB($\dot{\gamma}$) of 5% and (2) the working shear rate range is limited to $\dot{\gamma} \geq 0.1\ s^{-1}$ due to the downward flow of the silicone oil under gravity and induction of secondary flows at the imaged interface.

The working shear rate range is sufficient to partially probe the low shear plateau of the c = 40 mg/mL chitosan solution, which does not show flow instability or banding. Thus, although shear banding as a possibility cannot be fully eliminated in chitosan solutions, the lack of shear banded flow in the accessible region of the 40 mg/mL chitosan solution stress plateau indicates that shear banding alone is not an explanation for the stress plateau, and this phenomenon may instead be associated with yield stress behavior. To fully characterize the stress plateau, additional characterization techniques, like DLS, magnetic resonance or ultrasonic imaging

techniques may be helpful to overcome experimental challenges associated with imaging chitosan solutions.

Chapter 4
Characterization of the Active Motion of Colloids using Dynamic Light Scattering

4.1 Abstract

The active motion of colloidal particles has been previously characterized using optical microscopy coupled with particle tracking. The propulsion velocity (v*) is determined from the mean squared displacement (ΔL^2) of the colloids. In this study, platinum coated polystyrene microspheres are suspended in six dilute concentrations of hydrogen peroxide. These Janus particles undergo active motion by means of a self-diffusiophoretic mechanism driven by the catalytic decomposition of hydrogen peroxide into hydrogen and oxygen. We explore the characterization of v* by means of the complementary method of dynamic light scattering (DLS). The measured dynamic structure factor decays more steeply as hydrogen peroxide is added. This change in modality is suggestive of non-diffusive microdynamics and propulsion. A model that combines active motion with passive diffusion is developed to extract v* from the dynamic structure factor. To validate our methodology, v* from DLS measurements is compared to v* from direct measurements using optical microscopy and particle tracking. This comparison is limited, however, by anomalies in the optical microscopy and particle tracking data. However, external measurements of v* from confocal microscopy and particle tracking agree with v* determined from DLS measurements in this study. DLS offers advantages relative to optical microscopy because of the ease of application of DLS, and its applicability to particle sizes that are less than those resolvable by optical microscopy.

4.2 Introduction

The motion of colloidal particles of micron size and smaller is controlled by the effects of thermal fluctuations and viscous drag.[62] The result is translational and rotational Brownian motion. These dynamics are termed passive motion since particle trajectories exhibit stochastic motion. This passive motion is contrasted with particle systems that display active motion. In these systems, energy input into the system is converted to propulsive motion. The particles undergo dynamics in a sustained direction, as long as the energy input persists. The energy source can be chemical, as in the case of nano- or micromotors. Active motion can also be driven by externally applied fields or by flagella in bacteria.[63] Active motion combined with application specific surface functionalization may enable new technologies in a range of fields, including the self-repair of electrical circuits,[5] self-assembling artificial tissue,[6] and drug delivery.[7] Simple and accurate characterization of active motion is fundamental to the successful development of these applications.

Active colloidal motion has been characterized using microscopy coupled with particle tracking to extract the mean squared displacement (ΔL^2) of the ensemble of active paticles.[11–13] While simple in conception to execute, the utility of this methodology is limited by three factors. First, particle tracking microscopy requires specialized equipment and image analysis tools. Second, it can only be applied to characterize dynamics in particles whose size are greater than limits imposed by optical resolution and image analysis. Third, the extracted ΔL^2 is two-dimensional which may not accurately describe the motion of active colloids in all applications, especially those in bulk solution.[76] Further, extracting the propulsive velocity (v^*) from ΔL^2 requires accessing the short time region of ΔL^2 below the rotational diffusion time (τ_R) where τ

$<< \tau_R$ and τ is the lag time.[11] For smaller active colloids, this may be difficult or even experimentally limiting as as $\tau_R \sim R^3$ and sufficiently short times may be difficult or impossible to access given the frame acquisition rates of cameras and detectors typically used.[65]

Other techniques have been used to characterize the active motion of motile bacteria and spermatozoa including dynamic light scattering (DLS)[77–79,130–133] and differential dynamic microscopy (DDM).[134,135] In DDM the intensities of a time series of images is converted to Fourier space to extract characteristic time constants from the dynamic structure factor, $f(q,\tau)$, where q is the wave vector.[136] In DLS, temporal fluctuations in scattered light are measured by a detector and correlated to extract $f(q,\tau)$. By assuming the distribution of the propulsive velocities P(v), v* can be extracted from $f(q,\tau)$.[130,132–135] To date, the DLS characterization of active colloids has been limited to accessing bulk changes in the effective diffusivity using a zetasizer.[68]

The purpose of this paper is to address the gap in tools used to characterize active motion by showing that DLS can be used to extract v* from $f(q,\tau)$. In this paper, we fabricate synthetic micromotors by coating one side of polystyrene microspheres of diameter d = 1 μm and d = 0.5 μm with platinum. The platinum catalyzes the conversion of H_2O_2 into oxygen and water, and the resulting concentration gradient drives self-diffusiophoresis. In this study, we extract v* using both DLS and confocal microscopy with particle tracking. The utility of direct comparison of v* was limited by anomalies in the collected confocal microscopy data. However, v* from DLS measurements is in agreement with v* from confocal microscopy and particle tracking in the literature. While direct measurement of v* using confocal microscopy and particle tracking is

necessary to validate our DLS methodology, the similarity of v* with external work suggests that DLS is a viable tool for the characterization of v* warranting direct validation.

4.3 Experimental Methods

4.3.1 Janus Sphere Synthesis

Aqueous suspensions of d = 1.0 μm carboxyl latex microspheres, d = 0.5 μm carboxylate latex microspheres, and dyed d = 1.0 μm carboxyl latex microspheres from Thermo Fischer Scientific were used as received. After sonication for 10 minutes, the microspheres were washed three times via centrifugation and suspended in ethanol. A monolayer of particles was deposited on a glass substrate by spin coating the solution using a Laurell Technologies Corporation (Model WS-650MZ-23NPPB) spin-coater. A single layer of 10 nm platinum was deposited on the monolayer through physical vapor deposition using an Enerjet Evaporator at the Laurie Nanofabrication Facility at the University of Michigan. After a minimum of 24 hours, particles were recovered through gentle mechanical abrasion with 18.2 MΩ Millipore water. The concentration of the resulting solutions was measured using a hemocytometer (Fisher Scientific). For the undyed Janus microsphere solutions, the concentration was 0.00052 vol. % for d = 1.0 μm and 0.00215 vol.% for d = 0.5 μm. For the dyed Janus microsphere solution of d = 1.0 μm, the concentration was found to be 0.00205 vol. %. Janus microsphere synthesis and characterization was performed by Keara Saud.

4.3.2 Dynamic Light Scattering

Dynamic light scattering (DLS) was performed using a compact goniometer system (CGS-3, ALV GmbH, Langen, Germany) with a multi-tau digital correlator (ALV/LSE-5004,

ALV GmbH, Langen, Germany). For DLS, the minimum decay time of the correlator was 25 ns. All measurements were done at room temperature. A laser with wavelength λ_0 = 632.8 nm (Model 1145P HeNe laser, JDSU, California) was used at a single angle θ = 20°, which corresponds to a scattering vector q = 4.59 μm^{-1}, where $q = 4\pi n \sin(\theta/2)/\lambda_0$; n is the refractive index of the solvent.

The selection of θ = 20° was optimal experimentally as the measured scattering intensity was highest at this angle. Thus, the concentration of Janus microspheres and resulting generated oxygen could be minimized. Additionally, Mie scattering necessitated measurement at low angles for d = 1.0 μm, as the measured intensity of scattered light was too low at θ > 20°. Janus microsphere solutions were prepared of c = 5.2×10^{-8} vol.% for d = 1.0 μm and c = 1.2×10^{-7} vol.% for d = 0.5 μm. At these concentrations, the solutions are within the dilute regime but of sufficient concentration to avoid fluctuations in the measured intensity from the number of particles in the scattering volume in the dilute limit.[40] The measured intensity of scattered light at θ = 20° for both concentrations is greater than 1,000 kHz without attenuation.

Sample vials were pre-cleaned by sonication in HPLC grade ethanol-water solution and in triple filtered (d = 0.02 μm, Whatman Anatop) HPLC grade acetone solution. Oxygen bubble formation is an experimental limitation, because these bubbles will scatter and thereby contribute to the DLS signal intensity. To suppress the potential for oxygen bubble formation, we designed an oxygen sink to scavenge generated oxygen from solution. The sink was produced from a cross-linked polydimethylsiloxane (PDMS) gel formed in the bottom of DLS vials. The gel was produced from the Dow SYLGARD™ 184 Encapsulant Clear Kit in which an elastomer base is

cross-linked with an elastomer curing agent. PDMS has been previously used to mitigate bubble formation in active colloid systems;[66] it prevents the nucleation and growth of oxygen bubbles by acting as an oxygen sink.[137] To form the gel, ~0.3 mL of un-cured gel was carefully pipetted into the bottom of the sample vial below the scattering volume and heated at 100°C for 40 minutes. The height of the PDMS gel was below the laser line. With the PDMS gel, no bubbles nucleated within the experimental time of ~ 5 minutes.

The normalized intensity autocorrelation function was computed by the instrument correlator from fluctuations in the intensity of light $I(q,\tau)_T$ as $g_2(q,\ \tau) = \langle I_T(q,\tau)I_T(q,0)\rangle / \langle I(q,\tau)\rangle_T^2$. The dynamic structure factor was obtained from $g_2(q, \tau)$ through the Seigert relation $g_2(q,\tau) = 1 + \beta|f(q,\tau)|^2$, where β is the coherence factor determined by extrapolating $g_2(q,\tau)$ to $\tau = 0$ for $\tau < 600$ ms. Reported data are the average of five 40 s runs performed on five separately prepared samples for a total of twenty-five runs per hydrogen peroxide concentration. Runs analyzed were those collected that were free of spurious spikes in the count rate; these spikes are likely the result of excess substrate platinum removed during mechanical abrasion and rarely appear in the scattering volume. All error bars represent standard error of the mean.

Hydrogen peroxide concentrations of 0%, 1%, 2%, 5%, 7% and 10% were prepared by adding concentrated 30 wt.% hydrogen peroxide solution (certified ACS, Fisher Chemical) to aqueous Janus solutions such that the volume of the final solution was 0.5 mL. Solutions were mechanically mixed for ~ 5 seconds to ensure complete mixing and immediately analyzed.

4.3.3 Confocal microscopy and particle tracking

Dynamic measurements of dilute solutions of Janus microspheres of d = 1.0 μm were collected with a confocal laser-scanning microscope (Nikon A1Rsi, NA = 1.4, 100x objective). Solution volumes of 100 μL were imaged in an 8 well chamber (Thermo Fisher Scientific) at room temperature. Hydrogen peroxide concentrations of 0%, 1%, 2%, 5%, 7% and 10% were prepared by adding concentrated 50 wt.% hydrogen peroxide solution (certified ACS, Fisher Chemical) to aqueous Janus solutions. Solutions were mechanically mixed by tilting the well in four directions for ~ 30 s. The concentration of Janus microspheres was 6.8×10^{-7} vol.%.

Particle sticking was significant at hydrogen peroxide concentrations greater than 5 vol. % in untreated wells. To eliminate sticking, wells were pre-treated with a thirty minute base bath (1 N potassium hydroxide in ethanol, Fisher Scientific), twenty minute UV and ozone treatment (UVO CLEANER Model 42, Jetlight Company, Inc.), and coated in poly(sodium 4-styrenesulfonate) (PSS – Fisher Scientific). To coat the wells in PSS, ~500 μL of a freshly prepared aqueous 0.05 mg/mL PSS solution soaked in wells for thirty minutes. The bulk of the solution was removed by pipette and residual solution was dried with pressurized air. Experiments were performed immediately after pre-treatment.

The frame size collected in dynamic measurements was 512 x 512 pixels, and the pixel size was 83 nm. To image the biphasic microspheres, two lasers of wavelength $\lambda = 561$ nm and $\lambda = 488$ nm were used to image the fluorescent polystyrene and reflective platinum coating respectively. Dynamic measurements were collected for 60 s at a frame rate of 15 fps. Occasional bubble formation was apparent at higher H_2O_2 concentrations directly and indirectly

though large and unidirectional currents; data with these features was discarded and recollected. The mean squared displacement of Janus microspheres was determined from dynamic measurements using TrackPy, a Python implementation of the Crocker and Grier algorithm.[138,139] The reported ΔL^2 is the average of data from five videos on each of five separately prepared samples.

4.4 Results

4.4.1 DLS Data

Figure 4.1 displays $f(q,\tau)$ for two sizes of active Janus microspheres and six hydrogen peroxide concentrations. For both d = 1.0 μm and d = 0.5 μm, $f(q,\tau)$ of the passive case (no H_2O_2) decays exponentially. As the concentration of hydrogen peroxide is increased, we observe a steeper decay at progressively shorter lag times. This change is especially apparent at low hydrogen peroxide concentrations, such that the difference between $f(q,\tau)$ for 5-10% H_2O_2 is significantly less than the difference between that of 0-5% H_2O_2. The strong dependence of $f(q,\tau)$ on hydrogen peroxide concentration supports the validity of DLS as an experimental tool to probe the active motion of colloids.

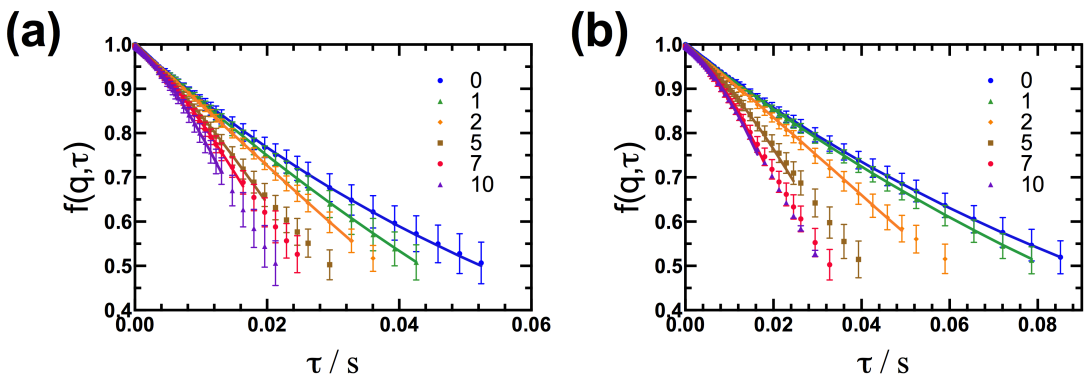

Figure 4.1 f(q,τ) for Janus microspheres of d = 0.5 um (a) and d = 1.0 um (b) in six hydrogen peroxide concentrations.
Lines show fits using Eqn. 5, discussed in the next section.

4.4.2 Analysis of DLS Spectra

For a monodisperse solution of free spherical colloids undergoing Brownian diffusion, the dynamic structure factor can be modeled using Eqn. 1 where D is the diffusivity.

$$f(q,\tau) = e^{-Dq^2\tau} \qquad \text{Eqn. 1}$$

In contrast, in active systems where the contribution of active motion is significantly greater than the diffusive contribution, the Brownian contribution to motion becomes insignificant and the dynamic structure factor can be modeled using Eqn. 2.[40]

$$f(q,\tau) = \int_0^\infty P(v)\frac{sin(qv\tau)}{qv\tau}dv \qquad \text{Eqn. 2}$$

Where both Brownian and active motion both contribute to the displacement of a particle, the dynamic structure factor can be modeled as the product of Eqn. 1 an Eqn. 2:[134]

$$f(q,\tau) = e^{-Dq^2\tau} \int_0^\infty P(v) \frac{sin(qv\tau)}{qv\tau} dv \qquad \text{Eqn. 3}$$

The functional form of P(v) is system dependent. In previous studies of bacterial active motion, significant polydispersity necessitated the use of velocity distributions to account for polydispersity. In the present situation, we assume the velocity distribution is sharply peaked around a characteristic value, and therefore represent the velocity distribution as a single propulsive velocity, v*, using a delta function $P(v) = \delta(v - v^*)$. By evaluating Eqn. 3 using the assumed P(v), we arrive at $f(q,\tau)$ in terms of v* and D in Eqn. 4 below.

$$f(q,\tau) = e^{-Dq^2\tau} \frac{sin(qv^*\tau)}{qv^*\tau} \qquad \text{Eqn. 4}$$

If its argument is small, the sinc function in Eqn. 4 may be replaced with the leading terms of its Taylor series expansion, valid where $qv^*\tau < 1$, shown in Eqn. 5:

$$f(q,\tau) = e^{-Dq^2\tau} \left(1 - \frac{(qv^*\tau)^2}{6}\right) \qquad \text{Eqn. 5}$$

For the passive cases shown in Figure 4.1a and b, data were fit with Eqn. 1 to obtain D = 0.62 μm^2/s and D = 0.36 μm^2/s and coated diameters of 0.72 μm and 1.22 μm calculated using the Stokes-Einstein equation respectively. The passive case diffusivities obtained using Eqn. 1 were treated as constants in Eqn. 5. The data shown in Figure 4.1 for hydrogen peroxide

concentrations of 1-10 % were fit using Eqn. 5 over the range of τ where $qv^*\tau < 1$, as adjusted based on v* over 200 iterations such that a constant maximum τ and v* were attained.

The propulsive velocity as a funciton of hydrogen peroxide volume percent is shown in Figure 4.2. The propulsive velocity is consistantly higher in the smaller Janus microspheres. In fact, increasing the uncoated diameter of the polystyrene microsphere from 1.0 μm to 0.5 μm results in a decrease in v* of 30% on average over all hydrogen peroxide concentrations. For both populations of microsphere, v* increases with H_2O_2 concentration; this dependence is more pronounced at low than at high hydrogen peroxide concentrations. The decomposision of hydrogen peroxide on the platinum surface is governed by Michaelis-Menten reaction kinetics. The functionality of v* with hydrogen peroxide is consistent with these kinetics as well as with previous observations by Howse et al.[11]

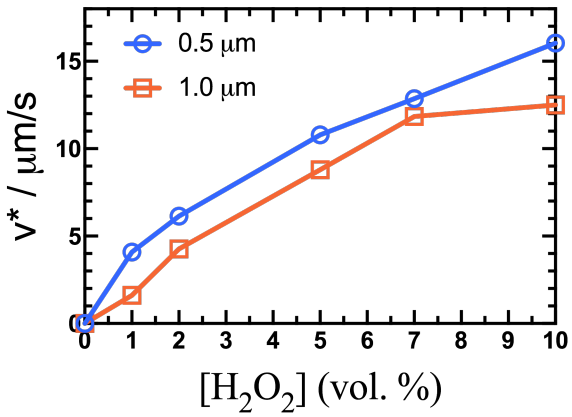

Figure 4.2 The propolsive velocity v* as a function of hydrogen peroxide volume percent [H_2O_2] for two Janus microspheres of d = 0.5 um and d = 1.0 um as extracted from Eqn. 5.

4.4.3 Confocal microscopy and particle tracking

The mean squared displacement was calculated from videos of fluorescent Janus microspheres of uncoated d = 1.0 μm. For six concentrations of hydrogen peroxide, ΔL^2 is shown in Figure 4.3a. The passive case displays the expected linear functionality of $\Delta L^2(\tau) = 4D\tau$ with D = 0.33 $\mu m^2/s$. The diffusivity is consistent with d = 1.3 μm using the Stokes-Einstein relation.

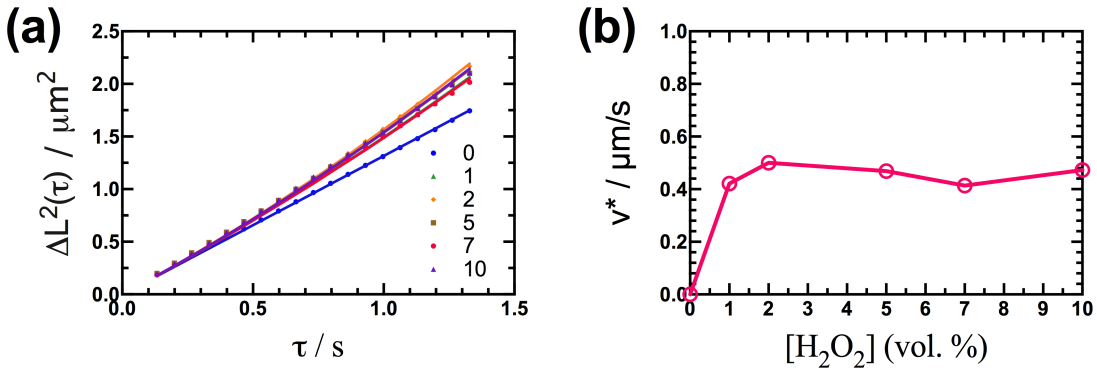

Figure 4.3 Mean square displacement and extracted v*.
(a) ΔL^2 of Janus microspheres (d = 1.0 μm) with six concentrations of H_2O_2 from 0 – 10 vol. % as obtained from confocal microscopy and particle tracking. Lines show fits using Eqn. 6 for $\tau < \tau_R$. (b) v* from fits shown in (a) using Eqn. 6.

With added hydrogen peroxide, ΔL^2 shows a stronger dependence on time, increasing more quickly than in the passive case. Unlike previous reports,[11,66] ΔL^2 does not strongly depend on H_2O_2 vol. %. In fact, ΔL^2 displays very little change from 1 – 10 vol.% H_2O_2. With hydrogen peroxide, ΔL^2 can be modeled using Eqn. 6 as in Howse et al. for short lag times were $\tau < \tau_R$:[11]

$$\Delta L^2(\tau) = 4D\tau + v^{*2}\tau^2 \qquad \text{Eqn. 6}$$

Using D from the passive case (D = 0.33 $\mu m^2/s$) as a constant, v* was determined by fitting ΔL^2 in Figure 4.3a with Eqn. 6 for $\tau < \tau_R$. For particles of d = 1.3 μm, τ_R = 1.4 s from $\tau_R = 8\pi\eta R^3/k_BT$ where η is solvent viscosity, k_B is Boltzmann's constant, and T is temperature. The fits are shown in Figure 4.3a, and the extracted v* is shown in Figure 4.3b. Consistent with observed invariance of ΔL^2, v* is constant from 1 – 10 vol.% H_2O_2. For these active cases <v*> = 0.46 ± 0.08 μm/s. This value is anomalously low and inconsistent with previous work in the Solomon group[66] as well as in the literature.[11] The functional form of v* with [H_2O_2] is also unexpected, as the progressive increase predicted by Michaelis-Menten reaction kinetics is not observed.

4.5 Discussion

To validate DLS as an experimental technique for characterizing the active motion of Janus particles, we would directly compare v* extracted from DLS measurements to that obtained using confocal microscopy and particle tracking. However, in our case this comparison is complicated by anomalies in the measured ΔL^2 and extracted v* using confocal microscopy and particle tracking. First, ΔL^2 is not sensitive to hydrogen peroxide concentration in the region of 1-10 vol.% H_2O_2. Second, the extracted values of v* are anomalously low in the context of previous measurements in the literature.[11,65,66] Third, v* does not follow the expected functionality with hydrogen peroxide addition as predicted by Michaelis-Menten reaction kinetics.[11]

These observations provide suggestion that our confocal measurements are subject to experimental problems. While experimental problems were not apparent in completing these

experiments, two potential issues have been identified that may adversely affect our data. First, active particles have been found to become inactive ~1 month after fabrication. The functionality of this decline in activity is not currently known. The confocal measurements were performed ~1 week after particle fabrication, whereas DLS measurements were performed ~1 day after particle fabrication. It follows that the particles used for confocal microscopy measurements could be less active after only a week. Second, the PSS coating used to prevent sticking may degrade in the presence of hydrogen peroxide. A few aggregates of PSS were observed with the 488 nm laser at 10 vol.% H_2O_2. Tracked particles would experience a more viscous or uneven microenvironment if the PSS coating was destabilized by hydrogen peroxide. This coating was not used in an otherwise identical experimental methodology where higher v* values with the functionality predicted by Michaelis-Menten reaction kinetics were reported.[66]

To validate DLS as a tool for the characterization of the active motion of colloids, we instead look at literature measurements of platinum coated polystyrene Janus microspheres in hydrogen peroxide as well as theoretical predictions of v* as a function of particle size. While these comparisons provide important context, the final validation of DLS measurements for v* determination will come from direct experimental confirmation using confocal microscopy and particle tracking.

For platinum coated polystyrene microspheres in 10% hydrogen peroxide solutions, v* was extracted for varying particle diameters using microscopy and particle tracking by Ebbens et al.,[65] shown in Figure 4.4. The extracted values of v* for the 10% hydrogen peroxide cases (c.f. Figure 4.2) are also plotted in Figure 4.4 against R_h from the DLS characterization of passive

Janus microspheres. For both microsphere populations, the magnitude of v* as extracted from DLS measurements is in good agreement with that extracted from confocal microscopy. While this finding is encouraging, its significance is limited by potential differences in particle activity. For example, hypothetically if particle activity was lower than in Ebbens et al., v* from DLS measurements could be too high.

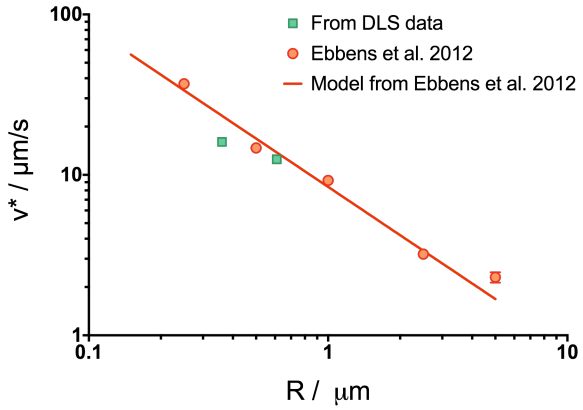

Figure 4.4 v* from DLS measurements in this work compared to literature.
v* from DLS measurements in this work is shown in green, and v* from microscopy and particle tracking from Ebbens et al. is shown in orange. All data corresponds to 10 wt.% H_2O_2.

The scaling of v* with particle size can be approximated as a function of effective Derjaguin length (λ_{eff}), concentration of fuel molecules in the bulk solution (C_∞), η, k_B, T, and R as shown in Eqn. 7.[65] Figure 4.4 shows Eqn. 7 with T = 293 K, $\eta = 1.0 \times 10^{-3}$ Pas, C_∞ = 10% w/v, and λ_{eff} = 0.62 Å as in Ebbens et al.[65]

$$v^* \simeq 0.3 \frac{k_B T \lambda_{eff}^2 C_\infty}{\eta R} \qquad \text{Eqn. 7}$$

On the basis of the measured R_h of the platinum coated Janus microspheres, increasing the uncoated polystyrene diameter from d = 0.5 μm to d = 1.0 μm results in an increase in coated particle radius of 41%. Eqn. 7 predicts an asymptotic dependence of v* on particle size of v* ~ 1/R. This simple relation predicts a decrease in v* of 29% as a result of increasing particle radius 41%. This predicted decrease is in agreement with the 30% decrease reported in v* for all hydrogen peroxide concentrations in this study. This agreement indicates that the v* extracted from DLS measurements is representative of the real v* of the Janus microspheres. This check doesn't validate the absolute magnitude of v*, however, as multiplication of v* by a constant, for example, would yield the same expected change in v* with R. Systemic deviation of v* determined from DLS and confocal microscopy by a constant pre-factor has been reported in systems of motile spermatozoa.[140]

4.6 Conclusions

Active motion combined with application specific surface functionalization may enable new technologies in a range of fields, including the self-repair of electrical circuits,[5] self-assembling artificial tissue,[6] and drug delivery.[7] Simple and accurate characterization of active motion is fundamental to successful development of these applications. In this manuscript we characterize the motion of active Janus microspheres using DLS and confocal microscopy with particle tracking. To date, the DLS characterization of active colloids has been limited to accessing bulk changes in the effective diffusivity using a zetasizer.[68] Two populations of Janus microspheres were fabricated by coating polystyrene microspheres of d = 0.5 μm and d =1.0 μm with platinum. The platinum catalyzes the conversion of H_2O_2 into oxygen and water, and the

resulting concentration gradient drives self-diffusiophoresis. In this study we consider six concentrations of hydrogen peroxide from 0 – 10 vol.%.

From DLS measurements, the dynamic structure factor $f(q,\tau)$ for both populations of Janus microspheres decays exponentially as expected for the passive case of 0 vol. % H_2O_2. With H_2O_2 addition, the decay becomes progressively steeper. A model was developed for $f(q,\tau)$ to account for both Brownian and active motion contributions. For the active motion contribution, we assume a uniform propulsive velocity v*. With increasing hydrogen peroxide concentration, v* increases with the expected functionality from Michaelis-Menten reaction kinetics.[11] The magnitude of v* is in agreement with that extracted from confocal microscopy and particle tracking externally by Ebbens et al.[65] Increasing the diameter of the uncoated polystyrene microsphere from d = 0.5 μm to d =1.0 μm resulted in a decrease in the average v* of 30% for all hydrogen peroxide concentrations. This decrease is in agreement with the predicted decrease of 29% from $v^* \sim 1/R$.[65]

The validity of v* from modeling $f(q,\tau)$ would be demonstrated by direct comparison with v* obtained through in-house confocal microscopy and particle tracking measurements. To this end, ΔL^2 for Janus microspheres (d = 1.0 μm) for six hydrogen peroxide concentrations was determined from confocal microscopy and particle tracking. However, the measured ΔL^2 and extracted v* are problematic in that ΔL^2 is not sensitive to hydrogen peroxide concentration in the region of 1-10 vol.% H_2O_2, and the extracted values of v* are anomalously low in the context of previous measurements.[11,65,66] Possible experimental sources of error include diminished particle activity and the instability of a PSS coating. These issues may be eliminated in future

confocal microscopy experiments by using un-aged particles and a piranha bath as a pretreatment as in Howse et al.[11] and Ebbens et al.[65] The comparison of v* with external work suggests that DLS is a viable tool for the characterization of v* warranting direct validation.

Chapter 5

Concluding Remarks and Future Directions

5.1 Conclusions

Mechanical rheometry and dynamic light scattering (DLS) were used to characterize solutions of chitosan. The steady shear rheology of chitosan solutions of c = 3-80 mg/mL display a region of shear thinning consistent with an apparent yield stress. The creep compliance of a c = 40 mg/mL chitosan solution shows a transition from elastic to viscous behavior with applied stress, consistent with the existence of a yield stress. Using DLS to probe the microstructure of concentrated and gelled chitosan solutions, we report slow relaxation dynamics consistent with the presence of a structured network or glassy fluid. The addition of urea, a disrupter of hydrogen bonds and hydrophobic effects, did not significantly alter the features of chitosan rheology but did reduce the apparent yield stress by ~30%.

Shear banding or other flow phenomena can occur in yield stress fluids in the region of the stress plateau of the steady shear flow curve. Chitosan solutions of c = 40 mg/mL and c = 65 mg/mL were characterized using fluorescence microscopy with time-resolved particle image velocimetry (PIV) to evaluate shear banded flow. Rapid laser-induced sample evaporation necessitated the application of external silicone oil. As a result, images were slightly distorted, and the slow downward flow of silicone oil under gravity induced a secondary flow at the chitosan boundary. As a result, our analysis was limited to shear rates of greater than $\dot{\gamma} = 0.01\ s^{-1}$. While the shear stress plateau was partially accessible for c = 40 mg/mL, it was not accessible in

the case of c = 65 mg/mL. Thus, the possibility of shear banding in the entire range of shear rates could not be evaluated; however, there does not appear to be shear banded flow in at least the limited range that is accessible experimentally.

Active Janus particles were fabricated by coating polystyrene particles, with diameters of 1.0 μm and 0.5 μm, with platinum. By catalyzing the decomposition of hydrogen peroxide at the platinum surface, the Janus particles generate chemical energy to sustain active motion through self-diffusiophoresis. The motion of active Janus colloids was characterized using a novel technique, DLS. The propulsive velocity (v*) was extracted for hydrogen peroxide concentrations of 0-10%. The propulsive velocity increased with hydrogen peroxide concentration in accordance with Michaelis-Menton enzyme kinetics. Increasing the diameter of the uncoated polystyrene microsphere from d = 0.5 μm to d =1.0 μm resulted in a decrease in the average v* of 30% for all hydrogen peroxide concentrations. This decrease is in agreement with the predicted decrease from v* ~ 1/R.

Ultimately, v* extracted from DLS measurements would be validated by agreement with v* from confocal microscopy and particle tracking. To this end, ΔL^2 for Janus microspheres (d = 1.0 μm) for six hydrogen peroxide concentrations was determined from confocal microscopy and particle tracking. However, the measured ΔL^2 and extracted v* are problematic in that ΔL^2 is not sensitive to hydrogen peroxide concentration in the region of 1-10 vol.% H_2O_2, and the extracted values of v* are anomalously low in the context of previous measurements.[6,10,23] Possible experimental sources of error include diminished particle activity and the instability of a PSS

coating. While direct validation remains an area of future work, these results are encouraging and suggest that DLS is a valid technique for characterizing the motion of active colloids.

5.2 Future Directions

In our study of the apparent yield stress in chitosan solutions, the nature of the interactions driving chitosan association was not fully understood. The partial ability of urea to decrease the yield stress provides suggestion that hydrophobic interactions and hydrogen bonding are not the sole drivers of chitosan self-association. Varying the molecular weight of chitosan could elucidate the significance of polymer entanglement. Further, the nature of interactions could be directly probed. It has been suggested that crystalline domains underlie chitosan association. By using x-ray diffraction on dissolved chitosan solutions, we could determine if crystalline glucosamine domains persist in the solvated state. Additional characterization with microscopy techniques like wet-STEM, which appears to preserve solution microstructure, may also be helpful.

To further evaluate shear banded flow in chitosan solutions, the working experimental range would need to be extended to lower shear rates. Measurements in the low shear rate region were not possible due to sample evaporation and the resulting distortion of flow from externally applied silicone oil. Sample evaporation may be better controlled in a methodology without lasers, such as nuclear magnetic resonance (NMR) microscopy or ultrasound velocimetry (USV).

Where there is great potential for future work is in the characterization of active colloid systems using DLS. First, DLS could enable the characterization of particles of even lower diameters than what is presented in Chapter 4. Second, alternative methods of active motion

induction that do not generate oxygen should be explored, including other chemical self-diffusiophoretic mechanisms and directed assembly. External fields for directed assembly could be fabricated inside the DLS unit. This would allow the characterization of DLS at long time scales and at maximum velocities without hindrance from bubble formation.

Third, the field of DLS characterization of active particles should be expanded to include anisotropic particles. Anisotropic particles may move dissimilarly in two vs. three dimensions. Microscopy-based tracking techniques often constrain the motion to two dimensions, and thus their relevance to three-dimensional technologies and applications may be limited. Thus, demonstrated characterization of and standard methodology for anisotropic particles using DLS would be a useful contribution to the field.

Fourth, DLS could be used to determine the effect of active particles embedded within a polymer or colloidal gel on the external gel microstructure. This analysis may be limited to transparent gels of, for example, gelatin, or require the utilization of diffuse wave spectroscopy (DWS), which is suitable for non-transparent samples. This project may be complimented by the development of in-device induced activity by external fields. The use of external fields would allow the activity to be turned on and off in a controlled manor without generating microstructure-damaging oxygen bubbles. Understanding how active particles embedded in a gel affect the surrounding gel microstructure may enable new technologies in drug delivery, medicine, and other fields.

References

1. Dash, M., Chiellini, F., Ottenbrite, R. M. & Chiellini, E. Chitosan - A versatile semi-synthetic polymer in biomedical applications. *Prog. Polym. Sci.* **36**, 981–1014 (2011).
2. Fall, A., Huang, N., Bertrand, F., Ovarlez, G. & Bonn, D. Shear thickening of cornstarch suspensions as a reentrant jamming transition. *Phys. Rev. Lett.* **100**, 1–4 (2008).
3. Tomihata, K. & Ikada, Y. In vitro and in vivo degradation of films of chitin and its deacetylated derivatives. *Biomaterials* **18**, 567–575 (1997).
4. Kean, T. & Thanou, M. Biodegradation, biodistribution and toxicity of chitosan. *Adv. Drug Deliv. Rev.* **62**, 3–11 (2010).
5. Li, J. *et al.* Self-Propelled Nanomotors Autonomously Seek and Repair Cracks. *Nano Lett.* **15**, 7077–7085 (2015).
6. Peng, F., Tu, Y. & Wilson, D. A. Micro/nanomotors towards: In vivo application: Cell, tissue and biofluid. *Chem. Soc. Rev.* **46**, 5289–5310 (2017).
7. Medina-Sánchez, M., Xu, H. & Schmidt, O. G. Micro- and nano-motors: The new generation of drug carriers. *Ther. Deliv.* **9**, 303–316 (2018).
8. Ebbens, S. J. Active colloids: Progress and challenges towards realising autonomous applications. *Curr. Opin. Colloid Interface Sci.* **21**, 14–23 (2016).
9. Korchagina, E. V. & Philippova, O. E. Multichain aggregates in dilute solutions of associating polyelectrolyte keeping a constant size at the increase in the chain length of individual macromolecules. *Biomacromolecules* **11**, 3457–3466 (2010).

10. Popa-Nita, S., Alcouffe, P., Rochas, C., David, L. & Domard, A. Continuum of structural organization from chitosan solutions to derived physical forms. *Biomacromolecules* **11**, 6–12 (2010).

11. Howse, J. R. *et al.* Self-Motile Colloidal Particles : From Directed Propulsion to Random Walk. **048102**, 8–11 (2007).

12. Szakasits, M. E., Zhang, W. & Solomon, M. J. Dynamics of Fractal Cluster Gels with Embedded Active Colloids. *Phys. Rev. Lett.* **119**, 1–5 (2017).

13. Palacci, J. *et al.* Light-activated self-propelled colloids. *Philos. Trans. R. Soc. A Math. Phys. Eng. Sci.* **372**, 20130372 (2014).

14. Park, J. W. & Park, K.-H. Acid-Base Equilibria and Related Properties of Chitosan. *Bull. Korean Chem. Soc.* **4**, 68–72 (1983).

15. Taghizadeh, S. M. & Davari, G. Preparation, characterization, and swelling behavior of N-acetylated and deacetylated chitosans. *Carbohydr. Polym.* **64**, 9–15 (2006).

16. Philippova, O. E. *et al.* Aggregation of some water-soluble derivatives of chitin in aqueous solutions: Role of the degree of acetylation and effect of hydrogen bond breaker. *Carbohydr. Polym.* **87**, 687–694 (2012).

17. Philippova, O. E. & Korchagina, E. V. Chitosan and Its Hydrophobic Derivatives: Preparation and Aggregation in Dilute Aqueous Solutions. *Polym. Sci. Ser. A* **54**, 552–572 (2012).

18. Rabea, E. I., Badawy, M. E.-T., Stevens, C. V., Smagghe, G. & Steurbaut, W. Chitosan as Antimicrobial Agent: Applications and Mode of Action. *Biomacromolecules* **4**, 1457–

1465 (2003).

19. Tikhonov, V. E. *et al.* Bactericidal and antifungal activities of a low molecular weight chitosan and its N-/2(3)-(dodec-2-enyl)succinoyl/-derivatives. *Carbohydr. Polym.* **64**, 66–72 (2006).

20. Roller, S. & Covill, N. The antifungal properties of chitosan in laboratory media and apple juice. *Int. J. Food Microbiol.* **47**, 67–77 (1999).

21. Agulló, E., Rodríguez, M. S., Ramos, V. & Albertengo, L. Present and Future Role of Chitin and Chitosan in Food. *Macromol. Biosci.* **3**, 521–530 (2003).

22. Jimtaisong, A. & Saewan, N. Utilization of carboxymethyl chitosan in cosmetics. *Int. J. Cosmet. Sci.* **36**, 12–21 (2014).

23. Aranaz, I. *et al.* Cosmetics and cosmeceutical applications of chitin, chitosan and their derivatives. *Polymers (Basel).* **10**, 213 (2018).

24. Liu, Z., Jiao, Y., Wang, Y., Zhou, C. & Zhang, Z. Polysaccharides-based nanoparticles as drug delivery systems. *Adv. Drug Deliv. Rev.* **60**, 1650–1662 (2008).

25. Crini, G. Recent developments in polysaccharide-based materials used as adsorbents in wastewater treatment. *Prog. Polym. Sci.* **30**, 38–70 (2005).

26. Yi, H. *et al.* Biofabrication with chitosan. *Biomacromolecules* **6**, 2881–2894 (2005).

27. Rao, S. B. & Sharma, C. P. Use of chitosan as a biomaterial: Studies on its safety and hemostatic potential. *J. Biomed. Mater. Res.* **34**, 21–28 (1997).

28. Dai, T., Tanaka, M., Huang, Y.-Y. & Hamblin, M. R. *Chitosan preparations for wounds and burns: antimicrobial and would-healing effects*. vol. 9 (2011).

29. Ueno, H., Mori, T. & Fujinaga, T. Topical formulations and wound healing applications of chitosan. *Adv. Drug Deliv. Rev.* **52**, 105–115 (2001).

30. Noel, S. P., Courtney, H., Bumgardner, J. D. & Haggard, W. O. Chitosan films: A potential local drug delivery system for antibiotics. *Clin. Orthop. Relat. Res.* **466**, 1377–1382 (2008).

31. Noel, S. P., Courtney, H. S., Bumgardner, J. D. & Haggard, W. O. Chitosan sponges to locally deliver amikacin and vancomycin: A pilot in vitro evaluation. *Clin. Orthop. Relat. Res.* **468**, 2074–2080 (2010).

32. Smith, J. K., Bumgardner, J. D., Courtney, H. S., Smeltzer, M. S. & Haggard, W. O. Antibiotic-loaded chitosan film for infection prevention: A preliminary in vitro characterization. *J. Biomed. Mater. Res. - Part B Appl. Biomater.* **94**, 203–211 (2010).

33. Aoyagi, S., Onishi, H. & Machida, Y. Novel chitosan wound dressing loaded with minocycline for the treatment of severe burn wounds. *Int. J. Pharm.* **330**, 138–145 (2007).

34. Greene, A. H., Bumgardner, J. D., Yang, Y., Moseley, J. & Haggard, W. O. Chitosan-coated stainless steel screws for fixation in contaminated fractures. *Clin. Orthop. Relat. Res.* **466**, 1699–1704 (2008).

35. Tunney, M. M., Brady, A. J., Buchanan, F., Newe, C. & Dunne, N. J. Incorporation of chitosan in acrylic bone cement: Effect on antibiotic release, bacterial biofilm formation and mechanical properties. *J. Mater. Sci. Mater. Med.* **19**, 1609–1615 (2008).

36. Wyss, H. M. Rheology of soft materials. in *Fluids, Colloids and Soft Materials: An Introduction to Soft Matter Physics* (eds. Fernandez□Nieves, A. & Puertas, A. M.) 149–

163 (John Wiley & Sons, Inc, 2016). doi:10.1002/9781119220510.

37. T.G. Mezger. *The Rheology Handbook: For Users of Rotational and Oscillatory Rheometers*. (Vincentz Network GmbH & Co KG, 2006).

38. Kjøniksen, A.-L., Iversen, C., Nyström, B., Nakken, T. & Palmgren, O. Light Scattering Study of Semidilute Aqueous Systems of Chitosan and Hydrophobically Modified Chitosans. *Macromolecules* **31**, 8142–8148 (1998).

39. Buhler, E. & Rinaudo, M. Structural and Dynamical Properties of Semirigid Polyelectrolyte Solutions: A Light-Scattering Study. *Macromolecules* **33**, 2098–2106 (2000).

40. Berne, B. J. & Pecora, R. *Dynamic Light Scattering With Applications to Chemistry, Biology, and Physics*. (Dover Publicatios Inc., 200AD).

41. Van Megen, W., Underwood, S. M. & Pusey, P. N. Nonergodicity parameters of colloidal glasses. *Phys. Rev. Lett.* **67**, 1586–1589 (1991).

42. Larson, R. G. *The Structure and Rheology of Complex Fluids*. (Oxford University Press, 1998).

43. Divoux, T., Fardin, M. A., Manneville, S. & Lerouge, S. Shear Banding of Complex Fluids. *Annu. Rev. Fluid Mech.* **48**, 81–103 (2016).

44. Wei, Y., Solomon, M. J. & Larson, R. G. Time-dependent shear rate inhomogeneities and shear bands in a thixotropic yield-stress fluid under transient shear. *Soft Matter* **15**, 7956–7967 (2019).

45. Gasbarro, N. M. & Solomon, M. J. Yield stress and rheology of a self-associating chitosan

solution. *Rheol. Acta* **2**, (2019).

46. Divoux, T., Grenard, V. & Manneville, S. Rheological hysteresis in soft glassy materials. *Phys. Rev. Lett.* **110**, 1–5 (2013).

47. Kuhn, M. R. Heterogeneity and patterning in the quasi-static behavior of granular materials. *Granul. Matter* **4**, 155–166 (2003).

48. Bonn, D., Denn, M. M., Berthier, L., Divoux, T. & Manneville, S. Yield stress materials in soft condensed matter. *Rev. Mod. Phys.* **89**, 035005(40) (2017).

49. Tang, H., Kochetkova, T., Kriegs, H., Dhont, J. K. G. & Lettinga, M. P. Shear-banding in entangled xanthan solutions: Tunable transition from sharp to broad shear-band interfaces. *Soft Matter* **14**, 826–836 (2018).

50. Manneville, S. Recent experimental probes of shear banding. *Rheol. Acta* **47**, 301–318 (2008).

51. Britton, M. M. & Callaghan, P. T. Two-Phase Shear Band Structures at Uniform Stress. *Phys. Rev. Lett.* **78**, 4930–4933 (1997).

52. Manneville, S., Bécu, L., Grondin, P. & Colin, A. High-frequency ultrasonic imaging: A spatio-temporal approach of rheology. *Colloids Surfaces A Physicochem. Eng. Asp.* **270–271**, 195–204 (2005).

53. Russel, W. B. *Colloidal Dispersions*. (Cambridge University Press, 1989).

54. Yang, Y. *et al.* Synthesis and assembly of colloidal cuboids with tunable shape biaxiality. *Nat. Commun.* **9**, 1–8 (2018).

55. Sugimoto, T., Khan, M. M. & Muramatsu, A. Preparation of monodisperse peanut-type α-

Fe2O3 particles from condensed ferric hydroxide gel. *Colloids Surfaces A Physicochem. Eng. Asp.* **70**, 167–169 (1993).

56. Sacanna, S. & Pine, D. J. Shape-anisotropic colloids: Building blocks for complex assemblies. *Curr. Opin. Colloid Interface Sci.* **16**, 96–105 (2011).

57. Geng, Y., Van Anders, G., Dodd, P. M., Dshemuchadse, J. & Glotzer, S. C. Engineering entropy for the inverse design of colloidal crystals from hard shapes. *Sci. Adv.* **5**, 1–7 (2019).

58. Caruso, F. Nanoengineering of particle surfaces. *Adv. Mater.* **13**, 11–22 (2001).

59. Brigger, I., Dubernet, C. & Couvreur, P. Nanoparticles in cancer therapy and diagnosis. *Adv. Drug Deliv. Rev.* **64**, 24–36 (2012).

60. Ferrando, R., Jellinek, J. & Johnston, R. L. Nanoalloys: From theory to applications of alloy clusters and nanoparticles. *Chem. Rev.* **108**, 845–910 (2008).

61. Poizot, P., Laruelle, S., Grugeon, S., Dupont, L. & Tarascon, J. Nano-sizedtransition-metaloxidesas negative-electrode materials for lithium-ion batteries. **407**, (2000).

62. Sanchez, S., Soler, L. & Katuri, J. Chemically powered micro- and nanomotors. *Angew. Chemie - Int. Ed.* **54**, 1414–1444 (2015).

63. Guix, M., Mayorga-Martinez, C. C. & Merkoçi, A. Nano/Micromotors in (Bio)chemical science applications. *Chem. Rev.* **114**, 6285–6322 (2014).

64. Kapral, R. Perspective: Nanomotors without moving parts that propel themselves in solution. *J. Chem. Phys.* **138**, (2013).

65. Ebbens, S., Tu, M. H., Howse, J. R. & Golestanian, R. Size dependence of the propulsion

velocity for catalytic Janus-sphere swimmers. *Phys. Rev. E - Stat. Nonlinear, Soft Matter Phys.* **85**, 1–4 (2012).

66. Szakasits, M. E., Saud, K. T., Mao, X. & Solomon, M. J. Rheological implications of embedded active matter in colloidal gels. *Soft Matter* **15**, 8012–8021 (2019).

67. Gao, Y., Kim, J. & Helgeson, M. E. Microdynamics and arrest of coarsening during spinodal decomposition in thermoreversible colloidal gels. *Soft Matter* **11**, 6360–6370 (2015).

68. Jannasch, A. *et al.* Enzyme-Powered Hollow Mesoporous Janus Nanomotors. *Nano Lett.* **15**, 7043–7050 (2015).

69. Baraban, L. *et al.* Catalytic Janus motors on microfluidic chip: Deterministic motion for targeted cargo delivery. *ACS Nano* **6**, 3383–3389 (2012).

70. Wang, W., Castro, L. A., Hoyos, M. & Mallouk, T. E. Autonomous motion of metallic microrods propelled by ultrasound. *ACS Nano* **6**, 6122–6132 (2012).

71. Boymelgreen, A., Yossifon, G. & Miloh, T. Propulsion of Active Colloids by Self-Induced Field Gradients. *Langmuir* **32**, 9540–9547 (2016).

72. Zöttl, A. & Stark, H. Emergent behavior in active colloids. *J. Phys. Condens. Matter* **28**, (2016).

73. Szakasits, M. Active Fractal Gels of Janus Colloids. (2015).

74. Das, S. *et al.* Boundaries can steer active Janus spheres. *Nat. Commun.* **6**, 1–10 (2015).

75. Lee, T. C. *et al.* Self-propelling nanomotors in the presence of strong Brownian forces. *Nano Lett.* **14**, 2407–2412 (2014).

76. Dupont, A. *et al.* Three-dimensional single-particle tracking in live cells: News from the third dimension. *New J. Phys.* **15**, (2013).

77. Nossal, R., Chen, S.-H. & Lai, C.-C. Use of laster scattering for quantitative determinatin of bacterial motility. *Opt. Commun.* **4**, 35–39 (1971).

78. Nossal, R. & Chen, S. Light scattering from motile bacteria. *J. Phys. Colloq.* **33**, C1-171-C1-176 (1972).

79. Shimizu, H. & Matsumoto, G. Light Scattering Study on Motile Spermatozoa. *IEEE Trans. Biomed. Eng.* **BME-24**, 153–157 (1977).

80. Muzzarelli, R. A. A. Biochemical significance of exogenous chitins and chitosans in animals and patients. *Carbohydr. Polym.* **20**, 7–16 (1993).

81. Lucchesi, L. & Xie, H. Wound dressing devices and methods. (2015).

82. Desbrières, J. Viscosity of Semiflexible Chitosan Solutions: Influence of Concentration, Temperature, and Role of Intermolecular Interactions. *Biomacromolecules* **3**, 342–349 (2002).

83. Cho, J., Heuzey, M., Bégin, A. & Carreau, P. J. Viscoelastic properties of chitosan solutions: Effect of concentration and ionic strength. *J. Food Eng.* **74**, 500–515 (2006).

84. Carreau, P. J., Cho, J. & Heuzey, M. Effect of urea on solution behavior and heat-induced gelation of chitosan- b -glycerophosphate. **63**, 507–518 (2006).

85. Payet, L., Ponton, A., Grossiord, J. L. & Agnely, F. Structural and rheological properties of chitosan semi-interpenetrated networks. *Eur. Phys. J. E* **32**, 109–118 (2010).

86. Hwang, J. K. & Shin, H. H. Rheological properties of chitosan solutions. *Korea-Australia*

Rheol. J. **12**, 175–179 (2001).

87. Jin, L. *et al.* Shear-induced self-thickening in chitosan-grafted polyacrylamide aqueous solution. *Soft Matter* **9**, 1835–1843 (2013).

88. Lapasin, R. & Pricl, S. Rheology of polysaccharide systems. in *Rheology of Industrial Polysaccharides: Theory and Applications* 250–494 (Springer Science & Business Media, 2012).

89. Ganesan, M., Knier, S., Younger, J. G. & Solomon, M. J. Associative and Entanglement Contributions to the Solution Rheology of a Bacterial Polysaccharide. *Macromolecules* **49**, 8313–8321 (2016).

90. Cho, J., Heuzey, M. C., Bégin, A. & Carreau, P. J. Effect of urea on solution behavior and heat-induced gelationof chitosan-β-glycerophosphate. *Carbohydr. Polym.* **63**, 507–518 (2006).

91. Philippova, O. E. *et al.* Two types of hydrophobic aggregates in aqueous solutions of chitosan and its hydrophobic derivative. *Biomacromolecules* **2**, 483–490 (2001).

92. Tsaih, M. L. & Chen, R. H. Effect of molecular weight and urea on the conformation of chitosan molecules in dilute solutions. *Int. J. Biol. Macromol.* **20**, 233–240 (1997).

93. Chen, R. H. & Tsaih, M. L. Urea-Induced Conformational Changes of Chitosan Molecules and the Shift of Break Point of Mark-Houwink Equation by Increasing Urea Concentration. *J. Appl. Polym. Sci.* **75**, 452–457 (2000).

94. Sogias, I. A., Khutoryanskiy, V. V. & Williams, A. C. Exploring the factors affecting the solubility of chitosan in water. *Macromol. Chem. Phys.* **211**, 426–433 (2010).

95. Ren, S. Z. & Sorensen, C. M. Relaxation in Gels: Analogies to alpha and beta Relaxation in Glasses. *Physical Review Letters* vol. 70 1727–1730 (1993).

96. de Morais, W. A., Pereira, M. R. & Fonseca, J. L. C. Characterization of gelification of chitosan solutions by dynamic light scattering. *Carbohydr. Polym.* **87**, 2376–2380 (2012).

97. Doench, I. *et al.* Injectable and gellable chitosan formulations filled with cellulose nanofibers for intervertebral disc tissue engineering. *Polymers (Basel).* **10**, (2018).

98. dos Santos, Z. M., Caroni, A. L. P. F., Pereira, M. R., da Silva, D. R. & Fonseca, J. L. C. Determination of deacetylation degree of chitosan: a comparison between conductometric titration and CHN elemental analysis. *Carbohydr. Res.* **344**, 2591–2595 (2009).

99. Barnes, H. A. A review of the slip (wall depletion) of polymer solutions, emulsions and particle suspensions in viscometers: its cause, character, and cure. *J. Nonnewton. Fluid Mech.* **56**, 221–251 (1995).

100. Møller, P. C. F., Fall, A. & Bonn, D. Origin of apparent viscosity in yield stress fluids below yielding. *EPL* **87**, 38004 (2009).

101. Rubinstein, M. & Colby, R. H. *Polymer Physics*. (Oxford, 2003).

102. Horinaka, J. I., Urabayashi, Y., Takigawa, T. & Ohmae, M. Entanglement network of chitin and chitosan in ionic liquid solutions. *J. Appl. Polym. Sci.* **130**, 2439–2443 (2013).

103. Berth, G. & Dautzenberg, H. The degree of acetylation of chitosans and its effect on the chain conformation in aqueous solution. *Carbohydr. Polym.* **47**, 39–51 (2002).

104. Eberle, A. P. R., Castañeda-Priego, R., Kim, J. M. & Wagner, N. J. Dynamical arrest, percolation, gelation, and glass formation in model nanoparticle dispersions with

thermoreversible adhesive interactions. *Langmuir* **28**, 1866–1878 (2012).

105. Winter, H. H. & Chambon, F. Analysis of Linear Viscoelasticity of a Crosslinking Polymer at the Gel Point. *J. Rheol. (N. Y. N. Y).* **30**, 367–382 (1986).

106. Koziol, M., Fischer, K. & Seiffert, S. Origin of the low-frequency plateau and the light-scattering slow mode in semidilute poly(ethylene glycol) solutions. *Soft Matter* **15**, 2666–2676 (2019).

107. Joosten, J. G. H., Geladé, E. T. F. & Pusey, P. N. Dynamic light scattering by nonergodic media: Brownian particles trapped in polyacrylamide gels. *Phys. Rev. A* **42**, 2161–2175 (1990).

108. Martínez-Ruvalcaba, A., Chornet, E. & Rodrigue, D. Steady-shear rheology of concentrated chitosan solutions. *J. Texture Stud.* **35**, 53–74 (2004).

109. Rodd, A. B., Dunstan, D. E. & Boger, D. V. Characterisation of xanthan gum solutions using dynamic light scattering and rheology. *Carbohydr. Polym.* **42**, 159–174 (2000).

110. Dobrynin, A. V, Colby, R. H. & Rubinstein, M. Scaling Theory of Polyelectrolyte Solutions. *Macromolecules* **28**, 1859–1871 (1995).

111. Rubinstein, M. & Semenov, A. N. Dynamics of entangled solutions of associating polymers. *Macromolecules* **34**, 1058–1068 (2001).

112. Heo, Y. & Larson, R. G. The scaling of zero-shear viscosities of semidilute polymer solutions with concentration. *J. Rheol. (N. Y. N. Y).* **49**, 1117 (2005).

113. Semenov, A. N. & Rubinstein, M. Dynamics of Entangled Associating Polymers with Large Aggregates. *Macromolecules* **35**, 4821–4837 (2002).

114. Piau, J. M. Carbopol gels: Elastoviscoplastic and slippery glasses made of individual swollen sponges. *J. Nonnewton. Fluid Mech.* **144**, 1–29 (2007).

115. Piau, J.-M., Dorget, M., Palierne, J.-F. & Pouchelon, A. Shear elasticity and yield stress of silica–silicone physical gels: Fractal approach. *J. Rheol. (N. Y. N. Y).* **43**, 305–314 (2002).

116. Krall, A. H. & Weitz, D. A. Internal Dynamics and Elasticity of Fractal Colloidal Gels. **1**, 2–5 (1998).

117. Mohraz, A. & Solomon, M. J. Orientation and rupture of fractal colloidal gels during start-up of steady shear flow. *J. Rheol. (N. Y. N. Y).* **49**, 657 (2005).

118. Carpineti, M. & Giglio, M. Transition from Semiorder to Disorder in the Aggregation of Dense Colloidal Solusions. *Phys. Rev. Lett.* **70**, 3828–3831 (1993).

119. de Gennes, P.-G. *Scaling Concepts in Polymer Physics*. (Cornell University Press, 1985).

120. Esquenet, C., Terech, P., Boué, F. & Buhler, E. Structural and rheological properties of hydrophobically modified polysaccharide associative networks. *Langmuir* **20**, 3583–3592 (2004).

121. Nyström, B., Kjøniksen, A.-L. L. Al & Iversen, C. Characterization of association phenomena in aqueous systems of chitosan of different hydrophobicity. *Adv. Colloid Interface Sci.* **79**, 81–103 (1999).

122. Augusto de Melo Marques, F. *et al.* Structural and microscopic relaxations in a colloidal glass. *Soft Matter* **11**, 466–471 (2015).

123. Cipelletti, L. *et al.* Universal non-diffusive slow dynamics in aging soft matter. *Faraday Discuss.* **123**, 237–251 (2003).

124. Cheng, D. C.-H. Yield stress: A time-dependent property and how to measure it. *Rheol. Acta* **23**, 542–554 (1986).

125. Ovarlez, G., Cohen-Addad, S., Krishan, K., Goyon, J. & Coussot, P. On the existence of a simple yield stress fluid behavior. *J. Nonnewton. Fluid Mech.* **193**, 68–79 (2013).

126. Mair, R. W. & Callaghan, P. T. Observation of shear banding in worm-like micelles by NMR velocity imaging. *Europhys. Lett.* **36**, 719–724 (1996).

127. Kim, Y., Adams, A., Hartt, W. H., Larson, R. G. & Solomon, M. J. Journal of Non-Newtonian Fluid Mechanics Transient , near-wall shear-band dynamics in channel flow of wormlike micelle solutions. **232**, 77–87 (2016).

128. Méndez-Sánchez, A. F. *et al.* Particle image velocimetry of the unstable capillary flow of a micellar solution. *J. Rheol. (N. Y. N. Y).* **47**, 1455–1466 (2003).

129. Manneville, S., Bécu, L. & Colin, A. High-frequency ultrasonic speckle velocimetry in sheared complex fluids. *EPJ Appl. Phys.* **28**, 361–373 (2004).

130. Holz, M. & Chen, S.-H. Rotational–translational models for interpretation of quasi-elastic light scattering spectra of motile bacteria. *Appl. Opt.* **17**, 3197 (1978).

131. Rigler, R. & Thyberg, P. Rotational and translational swimming of human spermatozoa: A dynamic laser light scattering study. *Cytometry* **5**, 327–332 (1984).

132. Hallett, F. R., Craig, T. & Marsh, J. Swimming speed distributions of bull spermatozoa as determined by quasi-elastic light scattering. *Biophys. J.* **21**, 203–216 (1978).

133. Nossal, R. Spectral Analysis of Laser Light Scattered from Motile Microorganisms. *Biophys. J.* **11**, 341–354 (1971).

134. Wilson, L. G. *et al.* Differential dynamic microscopy of bacterial motility. *Phys. Rev. Lett.* **106**, 7–10 (2011).

135. Germain, D., Leocmach, M. & Gibaud, T. Differential dynamic microscopy to characterize Brownian motion and bacteria motility. *Am. J. Phys.* **84**, 202–210 (2016).

136. Giavazzi, F., Brogioli, D., Trappe, V., Bellini, T. & Cerbino, R. Scattering information obtained by optical microscopy: Differential dynamic microscopy and beyond. *Phys. Rev. E - Stat. Nonlinear, Soft Matter Phys.* **80**, 1–15 (2009).

137. Dendukuri, D., Pregibon, D. C., Collins, J., Hatton, T. A. & Doyle, P. S. Continuous-flow lithography for high-throughput microparticle synthesis. *Nat. Mater.* **5**, 365–369 (2006).

138. Crocker, J. C. & Grier, D. G. Methods of digital video microscopy for colloidal studies. *J. Colloid Interface Sci.* **179**, 298–310 (1996).

139. Allan, D. *et al.* soft-matter/trackpy: Trackpy v0.4.2. (2019) doi:10.5281/ZENODO.3492186.

140. Sattelle, D. B., Palmer, G. R. & Dott, H. Motility of bovine spermatozoa studied by laser light scattering. *Eur. Biophys. J.* **11**, 203–210 (1985).